Available online at www.sciencedirect.com
ScienceDirect
Comput. Methods Appl. Mech. Engrg. 370 (2020) 113279
Computer methods in applied mechanics and engineering
www.elsevier.com/locate/cma

Shape optimization of heterogeneous materials based on isogeometric boundary element method

Deyong Sun, Chunying Dong*

Department of Mechanics, School of Aerospace Engineering, Beijing Institute of Technology, Beijing 100081, China

Received 29 April 2020; received in revised form 6 July 2020; accepted 8 July 2020
Available online 15 July 2020

Abstract

In this paper, the isogeometric boundary element method (IGABEM) is used to optimize the shape of heterogeneous materials. In contrast to the isogeometric finite element method (IGAFEM), the iterative optimization algorithm based on IGABEM can be implemented directly from Computer-Aided Design (CAD) without returning the optimization results to CAD designers. The discontinuous element method is extended to IGABEM which deals with corner point problems of inhomogeneous materials. After the singularity of sensitivity analysis of boundary integral equations is demonstrated, the power series expansion method (PSEM) is applied to IGABEM to evaluate various degrees of singularity about sensitivity analysis, which shows more accuracy and efficiency than the element sub-division method (ESDM). A set of control points on the geometric boundary are chosen as design variables, which can be passed from the design model to the analysis model, and the objective function is the elastic energy increment. Finally, several numerical examples in 2D and 3D problems are presented to demonstrate the validity and robustness of the present method.

Keywords: Isogeometric boundary element method (IGABEM); Heterogeneous materials; Shape optimization; Elastic problem

1. Introduction

Finite element method (FEM) [1] and boundary element method (BEM) [2] are two standard numerical tools for the solutions of partial differential equations (PDE), especially in linear elastic problems [3]. The BEM has some appealing features in engineering simulation, such as reducing the dimensions by one, only discretizing the boundary, and automatically satisfying the boundary conditions at infinity, which provides an alternative to FEM. Only boundary discretization shows that BEM should be more attractive than domain discretization method, which occupies 80% of the total linear elastic problem solving time [4]. This method can be directly compatible with the computer-aided design (CAD) model without human intervention. However, the matrices of BEM are non-symmetric and dense, which restricts the efficiency of solving large-scale problems. In order to improve the computational efficiency of BEM, various accelerated algorithms have been adopted, such as Fast Multipole Method (FMM) [5], the wideband FMM [6], Adaptive Cross Approximation (ACA) [7], the fast wavelet transforms [8], and the precorrected fast Fourier transformation (FFT) [9].

* Corresponding author.
E-mail address: cydong@bit.edu.cn (C.Y. Dong).

https://doi.org/10.1016/j.cma.2020.113279

Shape optimization is a critical step for engineering design to obtain the optimal shape under the given objective functions and constrains. As a pace-setting technology, the regeneration of boundary shape is applied to the rational and automatic design process. Since the geometric models in CAD are descripted by the boundary, the mesh regeneration and boundary capture in domain are time-consuming and complex tasks in shape optimization.

In order to eliminate the gap between CAD and CAE, the isogeometric analysis (IGA) concept, which initially using Non-Uniform Rational B-splines (NURBS) to approximate the geometries and field variables, has been applied in shape optimization for its special advantages including [10]: (1) geometric exactness, (2) high order continuous fields, (3) flexible mesh refinement, such as knot-insertion (*h*-refinement), degree-elevation (*p*-refinement) or by *k*-refinement (high-degree and maximal smoothness), which can extend design model to analysis model. In the implementation of NURBS-based IGAFEM, Wall et al. [11] firstly used control points as design variables directly and considered the potential of boundary continuity control to trigger smooth or less smooth designs. Qian [12] proposed an approach to analytically calculate the full sensitivities of the positions and weights of control points, thus improving the flexibility of shape representation. Furthermore, NURBS-based IGAFEM has also been applied to shape optimization in the fields of fluid mechanics [13], electromagnetism [14] and heat conduction [15]. However, due to tensor product form of NURBS, NURBS-based IGAFEM has two critical drawbacks: (1) the complex geometry cannot be descripted by one NURBS patch, (2) the difficulty of local refinement wastes CPU time. In this paper, multi-patch NURBS surface is applied to construct complex geometry about heterogeneous materials, but it is difficult to avoid the interval and overlap between different patches. Several methods [16–22] have been proposed to alleviate those difficulties faced by initial IGA. And more details about IGA can be found in review papers [23,24].

In the implementation of IGABEM, the basic formulas of sensitivity of kernel functions were derived and applied to isogeometric shape optimization based on NURBS in [25]. IGABEM has also been used to carry out shape optimization in elastic problem [26] and acoustics [27,28]. Meanwhile, T-spline based IGABEM was used to shape optimization in fluid problem [19] and elastic problem [29]. It is worth noting that the regularized boundary integral equation is attractive to shape optimization of IGABEM for homogeneous materials because it reduces the order of singularity and avoids the sensitivity of the constant C dependent on the boundary continuity. However, most of the existing algorithms only consider the optimization of the position of the control points on the smooth boundary and consider the single domain problem, thus ignoring the corner point problem. This is also the potential limitation of shape optimization for IGABEM, which has been discussed for crack propagation [30,31]. In this paper, IGABEM for shape optimization of heterogeneous materials is proposed and applied to elastic heterogeneous materials.

Heterogeneous materials are ubiquitous in engineering structures. Due to the lack of fundamental solutions for general heterogeneous material problems, multi-domain boundary element method (MDBEM) [32] was used to solve such problems, in which the conditions of displacement continuity and traction equilibrium were used on the material interface. Recently, interface integral boundary element method (IIBEM) [33] has been proposed to study multi-domain problems in which the effect of nonhomogeneity between adjacent materials was embodied by the interface integrals. To the authors' knowledge, the use of gradient-based IGABEM optimization algorithm to optimize heterogeneous structure problems has not yet occurred.

However, in the implementation of both traditional BEM and IGABEM, the singularities on fundamental solutions appear when the distance between source point and field point approaches zero. Telles [34] proposed a self-adaptive algorithm to improve the accuracy of Gaussian quadrature approach within the near-singularity range. The rigid body displacement method [35] was developed to eliminate the singularity on collocation points corresponding to coefficient matrices. In this method, the elements in coefficient matrices must be calculated accurately except for the diagonal elements. The regularized form of boundary integral equation [36–38] can avoid calculation of strongly singular integrals and jump terms, but this method can only reduce the singularity order by one, and cannot completely avoid the hyper singularity. Hence, many strategies have been introduced to solve this problem, including new Gaussian quadrature approach [39], the local regularization method [40,41], transformation method [34,42,43], finite-part integral method [44], etc. The power series expansion method presented by Gao [45] was used to compute the singular integrals, whose orders are 1 to 6. And its applications can be found in [46]. In this paper, the power series expansion method is extended to shape optimization of 3D IGABEM to compute the singular integrals.

In this paper, the shape optimization of linear elasticity is extended to two-dimensional and three-dimensional heterogeneous materials. Strain energy is an important parameter to characterize the properties of heterogeneous materials. This special parameter has many applications in evaluating mechanical properties of materials. For

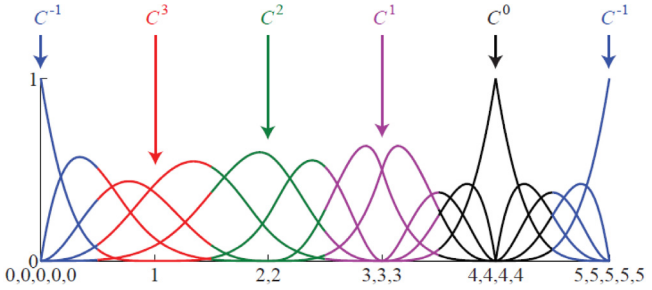

Fig. 1. NURBS basis functions.

martensitic transformation, the rate of transformations depends on the energy barrier or strain energy of the mixed microstructure of martensitic and austenite [47] tissues. Eshelby [48] proposed the analytic solutions of the spherical or ellipsoid inclusion stress field. The aim of shape optimization is to obtain maximum elastic energy increment under special constraints. The paper is organized as follows. In Section 2, the basic properties of NURBS are briefly introduced. Section 3 presented the procedure of multi-domain problems solved by IGABEM and the evaluation of singular boundary integral. Section 4 illustrates relevant shape optimization based on IGABEM, including maximization of elastic energy increment, and evaluation of strongly singular integral by the power series expansion method. In Section 5, the shape sensitivity analysis and error evaluation of cylindrical and spherical inclusions are introduced, and numerical examples are given. Section 6 shows some conclusions and future work.

2. Non-uniform rational B-splines (NURBS)

In the implementation of isogeometric analysis, NURBS plays a key role in the seamless integration of CAD and CAE by describing both physical and parametric spaces simultaneously. For completeness, this section briefly reviews some basic concepts of NURBS, and more details are accessible in [49].

A knot vector is a set of non-decreasing real number in the parametric space, which is the basis of NURBS, as shown below

$$\Xi = \{\xi_1, \xi_2, \ldots, \xi_{n+p+1}\}, \quad \xi_a \in \mathbb{R} \tag{1}$$

where a denotes the knot index, p is the curve order, and n is the number of basis functions or control points. The half open interval $[\xi_i, \xi_{i+1})$ is called a knot span.

With the concept of a knot vector, the B-spline basis functions are defined using the Cox–de Boor recursion formula

$$N_{a,0} = \begin{cases} 1, & \text{if } \xi_a \le \xi \le \xi_{a+1}. \\ 0, & \text{otherwise.} \end{cases} \tag{2}$$

for $p = 0$, and

$$N_{a,p}(\xi) = \frac{\xi - \xi_a}{\xi_{a+p} - \xi_a} N_{a,p-1}(\xi) + \frac{\xi_{a+p+1} - \xi}{\xi_{a+p+1} - \xi_{a+1}} N_{a+1,p-1}(\xi) \tag{3}$$

for $p = 1,2,3,\ldots$.

B-spline basis functions are C^∞ within elements and C^{p-m} on element boundary, where m is the number of knot repetitions (see Fig. 1). And it possesses several favorable properties such as local support, pointwise non-negativity, linear independence. As shown in Fig. 1, a whole B-spline curve can be defined by n basis functions in Eqs. (2) and (3) as well as control points $\mathbf{P}_a (a = 1, 2, \ldots, n)$.

The B-spline curve (see Fig. 2) can be constructed as a linear combination of B-spline basis functions and control points, i.e.

$$\mathbf{x}(\xi) = \sum_{i=1}^{n} N_{a,p}(\xi) \mathbf{P}_a \tag{4}$$

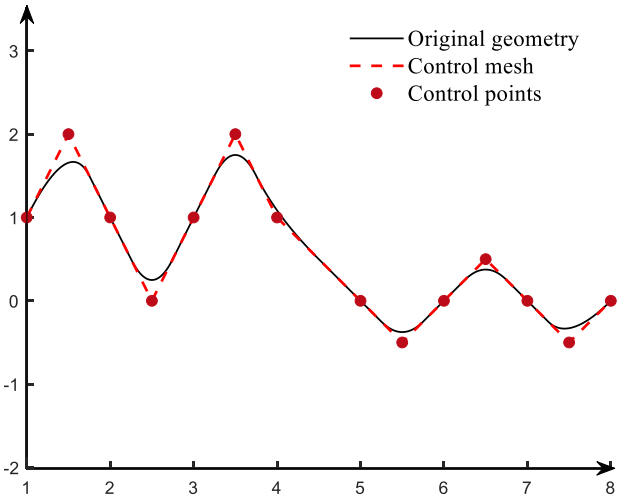

Fig. 2. B-spline curve. The knot vector is Ξ = {0, 0, 0, 1, 2, 3, 4, 5, ..., 11, 12, 12, 12}, and the control points are **P** = {(1, 1), (1.5, 2), (2, 1), (2.5, 0), (3, 1), (3.5, 2), (4, 1), (5, 0), (5.5, −0.5), (6, 0), (6.5, 0.5), (7, 0), (7.5, −0.5), (8, 0)}.

where the coefficients $\mathbf{P}_a$ denote the coordinates of control points, and $\mathbf{x} = (x, y, z)$ is the location of the physical space corresponding to the coordinate ξ in parametric space. To construct B-splines surface and solid, the basis functions can be obtained from the tensor product. B-spline surface basis function is given by

$$N_a(\xi|\Xi_a) \equiv \prod_{i=1}^{d_p} N_a^i(\xi_a^i|\Xi_a^i) \tag{5}$$

where i denotes the direction index, d_p is the number of dimensions.

Given a control net consisting of the control points $\mathbf{P}_{i,j}$, the B-spline surface can be constructed with tensor product property with knot vectors $\Xi = \{\xi_1, \xi_2, \ldots, \xi_{n+p+1}\}$ and $\Re = \{\eta_1, \eta_2, \ldots, \eta_{m+q+1}\}$,

$$\mathbf{x}(\xi, \eta) = \sum_{a=1}^{n}\sum_{b=1}^{m} N_{a,p}(\xi)N_{b,q}(\eta)\mathbf{P}_{a,b} \tag{6}$$

where n and m are number of basis functions in each dimension, respectively. p and q are the orders of B-spline basis functions corresponding to knot vectors Ξ and $\Re$.

NURBS are the extension of B-spline by assigning a positive weight ω_a to each basis function:

$$\mathbf{x}(\xi) = \sum_{a=1}^{n} R_{a,p}(\xi)\mathbf{P}_a \tag{7}$$

where $R_{a,p}$ are the NURBS basis functions, i.e.

$$R_{a,p}(\xi) = \frac{N_{a,p}(\xi)\omega_a}{W(\omega)} \tag{8}$$

with

$$W(\xi) = \sum_{a=1}^{n} N_{a,p}(\xi)\omega_a \tag{9}$$

The NURBS surface is defined using NURBS basis functions and control points under the same manner as B-spline surface,

$$R_a(\xi|\Xi_a) \equiv \prod_{i=1}^{d_p} R_a^i(\xi_a^i|\Xi_a^i) \tag{10}$$

And the NURBS surface in two dimensions can be shown as follows,

$$\mathbf{x}(\xi,\eta)=\sum_{a=1}^{n}\sum_{b=1}^{m}R_{a,p}(\xi)R_{b,q}(\eta)\mathbf{P}_{a,b} \tag{11}$$

If weights are all set to one, Eqs. (7) and (11) can be degenerated to Eqs. (4) and (6), respectively. Using NURBS, we can represent easily circular arcs and other conic sections.

For simplicity, in the following the geometries in isogeometric analysis can be descripted using global index A,

$$\mathbf{x}(\mathbf{s})=\sum_{A=1}^{N_A}R_A(\mathbf{s})\mathbf{P}_A \tag{12}$$

where N_A means the total number of control points and is equal to $n\times m$, $\mathbf{s}$ denotes the vector form of spatial coordinates in parametric space, hence $\mathbf{s}=\xi$ in 2D problems and $\mathbf{s}=(\xi,\eta)$ in 3D.

3. IGABEM for elastic problems

3.1. Boundary integral equations

The Boundary Element Method (BEM) is a powerful tool for solving a series of engineering problems, in which the partial differential equation (PDE) can be reformulated as boundary integral equation by Green's function, and the boundary integral equation only needs to solve the unknown fields on the boundary. In the present work, we apply this method to solve elastic problems. Consider an arbitrary domain Ω whose boundary $S\equiv\partial\Omega$, in the absence of body forces, the discrete form of displacement boundary integral equation (DBIE) for linear elastic problems is formulated as [50]

$$\mathbf{C}(\mathbf{x})\mathbf{u}(\mathbf{x})=\int_S\mathbf{U}(\mathbf{x},\mathbf{y})\mathbf{t}(\mathbf{y})dS-\int_S\mathbf{T}(\mathbf{x},\mathbf{y})\mathbf{u}(\mathbf{y})dS \tag{13}$$

where S is the boundary of domain, $\mathbf{x}$ and $\mathbf{y}$ are the source point and field point on the boundary, respectively. $\mathbf{C}(\mathbf{x})$ is a free coefficient matrix depending on the boundary smooth at source point (collocation point). $\mathbf{u}$ and $\mathbf{t}$ mean the displacement and traction vectors, respectively. $\mathbf{U}(\mathbf{x},\mathbf{y})$ and $\mathbf{T}(\mathbf{x},\mathbf{y})$ are the fundamental solutions of linear elastic problems, which are given as [51].

In 2D problems:

$$U_{ij}(\mathbf{x},\mathbf{y})=\frac{1}{8\pi\mu(1-v)}[(3-4v)\ln\frac{1}{r}\delta_{ij}+r_{,i}r_{,j}] \tag{14}$$

$$T_{ij}(\mathbf{x},\mathbf{y})=-\frac{1}{4\pi(1-v)r}[r_{,n}((1-2v)\delta_{ij}+2r_{,i}r_{,j})+(1-2v)(n_jr_{,i}-n_ir_{,j})] \tag{15}$$

In 3D problems:

$$U_{ij}(\mathbf{x},\mathbf{y})=\frac{1}{16\pi\mu(1-v)r}[(3-4v)\delta_{ij}+r_{,i}r_{,j}] \tag{16}$$

$$T_{ij}(\mathbf{x},\mathbf{y})=-\frac{1}{8\pi(1-v)r^2}[r_{,n}((1-2v)\delta_{ij}+3r_{,i}r_{,j})+(1-2v)(n_jr_{,i}-n_ir_{,j})] \tag{17}$$

where n_i is the unit normal component on x_i direction, and $r=|\mathbf{x}\text{-}\mathbf{y}|$ is the distance between source point and field point, and $r_{,i}=\frac{\partial r}{\partial x_i}$ is the partial derivative in ith direction. v is Poisson's ratio, μ is the shear modulus, and δ_{ij} is the Kronecker delta. Note that the kernel function U is weak singularity, and the kernel function T is strong singularity.

For infinite domain problem or multi-domain problem that the size of one is much bigger than others, the boundary integral equation is formulated as follows [52]

$$\mathbf{C}(\mathbf{x})\mathbf{u}(\mathbf{x})=\mathbf{u}^{\mathbf{0}}(\mathbf{x})+\int_S\mathbf{U}(\mathbf{x},\mathbf{y})\mathbf{t}(\mathbf{y})dS-\int_S\mathbf{T}(\mathbf{x},\mathbf{y})\mathbf{u}(\mathbf{y})dS \tag{18}$$

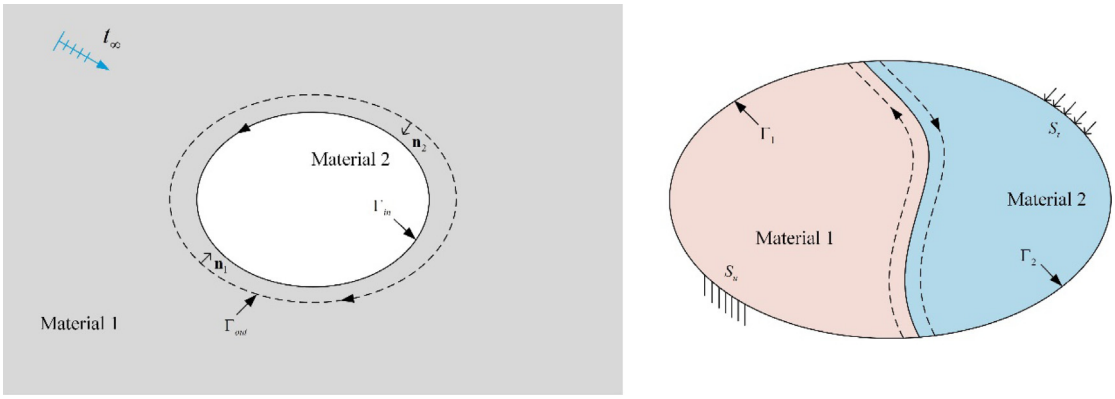

(a) Infinite domain problem. (b) Finite domain problem.

Fig. 3. Infinite and finite heterogeneous structures.

where $\mathbf{u}^{\mathbf{0}}(\mathbf{x})$ means the displacement vector at source point deriving from infinite traction boundary conditions. Thus, we can assemble Eqs. (13) and (18) as

$$\mathbf{C}(\mathbf{x})\mathbf{u}(\mathbf{x}) = B\mathbf{u}^{\mathbf{0}}(\mathbf{x}) + \int_S \mathbf{U}(\mathbf{x},\mathbf{y})\mathbf{t}(\mathbf{y})dS - \int_S \mathbf{T}(\mathbf{x},\mathbf{y})\mathbf{u}(\mathbf{y})dS \tag{19}$$

where $B = 1$ for infinite and $B = 0$ for finite domain problems.

3.2. Isogeometric boundary element method for heterogeneous structure

Heterogeneous structure solving by IGABEM is the critical step for engineering application, we divide the heterogeneous structures into two typical models as shown in Fig. 3.

In the implementation of isogeometric analysis, the geometry and field variables are described by NURBS or other splines simultaneously, which are different from conventional BEM. Consider one NURBS patch, the displacement and traction vectors around boundary are expressed using a NURBS expansion, i.e.

$$\mathbf{u}(\mathbf{s}) = \sum_{A=1}^{N_A} R_A(\mathbf{s})\widetilde{\mathbf{u}}_A \tag{20}$$

$$\mathbf{t}(\mathbf{s}) = \sum_{A=1}^{N_A} R_A(\mathbf{s})\widetilde{\mathbf{t}}_A \tag{21}$$

where $\widetilde{\mathbf{u}}_A, \widetilde{\mathbf{t}}_A$ are global displacement and traction parameters associated with control points by index A. Unlike conventional BEM, the NURBS basis functions do not obey Kronecker-delta property, so $\widetilde{\mathbf{u}}_A, \widetilde{\mathbf{t}}_A$ are not the actual displacement and traction around boundary. And the locations of collocation points (the projection of control points) will influence the stability and accuracy of numerical results. Simpson et al. [50] used Greville abscissae definition to acquire collocation points, which obtained reasonable and accurate results. Therefore, this method is used here.

According to Greville abscissae definition, the corresponding parameter of each collocation point is as follows:

$$\bar{\xi}_i = (\xi_i + \xi_{i+1} + \cdots \xi_{i+p})/p, i = 1, 2, \ldots, n \tag{22}$$

where p is the order of NURBS basis functions, and n is the number of control points in ξ direction.

In order to deal with the corner point problem in heterogeneous structure, we apply the discontinuous element method in IGABEM. The improved Greville abscissae definition (with improve coefficient $\beta = 0.5$) is given as follows [53]

$$\begin{cases} \bar{\xi}_1 = \bar{\xi}_1 + \beta(\bar{\xi}_2 - \bar{\xi}_1) \\ \bar{\xi}_n = \bar{\xi}_n - \beta(\bar{\xi}_n - \bar{\xi}_{n-1}) \end{cases} \tag{23}$$

If the boundary is discretized into E elements, then the discrete form of Eq. (19) is as follows

$$\mathbf{C}(\mathbf{x})\mathbf{u}(\mathbf{x}) = B\mathbf{u}^{\mathbf{0}}(\mathbf{x}) + \sum_{e=1}^{E}\int_{S_e}\mathbf{U}(\mathbf{x},\mathbf{y})\mathbf{t}(\mathbf{y})dS_e - \sum_{e=1}^{E}\int_{S_e}\mathbf{T}(\mathbf{x},\mathbf{y})\mathbf{u}(\mathbf{y})dS_e \tag{24}$$

Replacing the continuous fields using NURBS expansion in Eqs. (20) and (21), Eq. (24) is discretized as follows:

$$C_{ij}(\mathbf{x}(\mathbf{s}_p))\sum_{\alpha=1}^{N}R_\alpha^{\bar{e}}(\mathbf{s}_p)\widetilde{u}_j^{\bar{e}\alpha} = Bu_i^0(\mathbf{x}(\mathbf{s}_p)) + \sum_{e=1}^{E}\sum_{\alpha=1}^{N}P_{ij}^{e\alpha}(\mathbf{x},\mathbf{y})\widetilde{t}_j^{e\alpha} - \sum_{e=1}^{E}\sum_{\alpha=1}^{N}Q_{ij}^{e\alpha}(\mathbf{x},\mathbf{y})\widetilde{u}_j^{e\alpha} \tag{25}$$

where

$$P_{ij}^{e\alpha}(\mathbf{x},\mathbf{y}) = \int_{\mathbf{s}_e}U_{ij}(\mathbf{x}(\mathbf{s}_p),\mathbf{y}(\mathbf{s}_q))R_\alpha^e(\mathbf{s}_q)J\,d\mathbf{s}_e \tag{26}$$

$$Q_{ij}^{e\alpha}(\mathbf{x},\mathbf{y}) = \int_{\mathbf{s}_e}T_{ij}(\mathbf{x}(\mathbf{s}_p),\mathbf{y}(\mathbf{s}_q))R_\alpha^e(\mathbf{s}_q)J\,d\mathbf{s}_e \tag{27}$$

in which $\widetilde{u}_j^{e\alpha}$ and $\widetilde{t}_j^{e\alpha}$ are the jth components of displacement and traction locating on the α-th node of e-th element. N denotes the number of the control points corresponding to e-th element, and the subscripts p and q are the indexes of source and field points, and J is the Jacobian, which may be calculated by

$$J = \frac{d\Gamma}{d\mathbf{s}} \tag{28}$$

For each collocation point on the boundary, DBIE is applied to obtain the matrix form of the boundary integral equation as

$$\mathbf{H}\widetilde{\mathbf{u}} = B\mathbf{u}^0 + \mathbf{G}\widetilde{\mathbf{t}} \tag{29}$$

in which $\widetilde{\mathbf{u}}$ and $\widetilde{\mathbf{t}}$ are vectors containing displacement and traction nodal parameters on control points, and $\mathbf{u}^0$ denotes the displacement vector on collocation points derived from remote loading. $\mathbf{H}$ and $\mathbf{G}$ are the corresponding matrixes, whose entries are given as follows:

$$H_{ij}^{e\alpha} = C_{ij}(\mathbf{x}(\mathbf{s}_p))\sum_{\alpha=1}^{N}R_\alpha^e(\mathbf{s}_p) + \sum_{e=1}^{E}\sum_{\alpha=1}^{N}Q_{ij}^{e\alpha}(\mathbf{x}(\mathbf{s}_p),\mathbf{y}(\mathbf{s}_q)) \tag{30}$$

and

$$G_{ij}^{e\alpha} = \sum_{e=1}^{E}\sum_{\alpha=1}^{N}P_{ij}^{e\alpha}(\mathbf{x}(\mathbf{s}_p),\mathbf{y}(\mathbf{s}_q)) \tag{31}$$

The perfect interface is considered, that is, the displacement continuity ($\widetilde{\mathbf{u}}_1 = \widetilde{\mathbf{u}}_2$) and traction equilibrium ($\widetilde{\mathbf{t}}_1 = -\widetilde{\mathbf{t}}_2$) on the interface between the two materials remain, as shown in Fig. 3. The unknown displacement and traction variables can be solved from Eq. (32)

$$\begin{cases}\mathbf{H}_1\widetilde{\mathbf{u}}_1 = B\mathbf{u}^0 + \mathbf{G}_1\widetilde{\mathbf{t}}_1\\ \mathbf{H}_2\widetilde{\mathbf{u}}_2 = \mathbf{G}_2\widetilde{\mathbf{t}}_2\end{cases} \tag{32}$$

However, due to the opposite integral directions between two materials, the global index of A in coefficient matrices $\mathbf{H}_2$ and $\mathbf{G}_2$ must be converted into the same as those in $\mathbf{H}_1$ and $\mathbf{G}_1$. Assumed that the global index for material 1 is *A=(i-1)noPtsY+j*, then the global index for material 2 is *A=(noPtsX-i)noPtsY+j*, in which *noPtsX* and *noPtsY* are the numbers of control points in ξ and η directions, respectively. Therefore, Eq. (32) can be assembled as a total algebraic system as shown in [54,55] for heterogeneous materials,

$$\begin{bmatrix}\mathbf{H}_1\\ \mathbf{H}_2\end{bmatrix}[\widetilde{\mathbf{u}}_1] = \begin{bmatrix}\mathbf{B}\\ \mathbf{0}\end{bmatrix}[\mathbf{u}^0] + \begin{bmatrix}\mathbf{G}_1\\ -\mathbf{G}_2\end{bmatrix}[\widetilde{\mathbf{t}}_1] \tag{33}$$

in which $\mathbf{B}$ is a unit matrix when B=1 or null matrix when B=0.

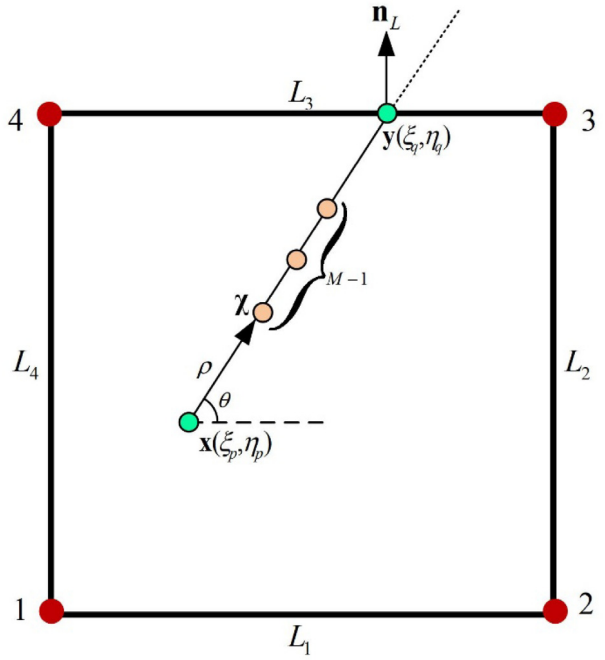

Fig. 4. Integral element in parametric domain.

3.3. Evaluation of singular boundary integrals

In the implementation of IGABEM, the accuracy of numerical calculation of singular integrals is the key and difficult point for the boundary element method to solve the problem successfully. Gauss–Legendre integral is the traditional and accurate method to calculate regular integrals. However, it will lose accuracy and stability when some singular integrals appear, such as weakly singular, strongly singular or hypersingular. In order to solve these problems, many methods have been provided. Simpson et al. [50,56] used Subtraction of Singularity Method (SST) and Telles transformation [34] to evaluate the strongly and weakly integrals appearing in 2D IGABEM, respectively. In order to eliminate the singularities in 3D IGABEM, the power series expansion method (PSEM) was employed [46], in which a surface integral was divided into a line integral over contour of the integration surface and a radial integral containing the singularities. The singularities condensed in the radial integral were removed analytically or numerically by extracting the finite value parts from the power series expansion.

Consider e-th element in Eq. (25) as shown in Fig. 4, $\mathbf{x}$ is the source point locating on the edge or domain of this element, and the singular integral is formulated in parametric space as

$$I^e(X) = \int_{S_e} \frac{\overline{f}(\mathbf{x},\mathbf{y})}{r^{\lambda}(\mathbf{x},\mathbf{y})} dS = \int_{-1}^{1}\int_{-1}^{1} \frac{\overline{f}(\mathbf{x},\mathbf{y})}{r^{\lambda}(\mathbf{x},\mathbf{y})} J_e d\xi d\eta \tag{34}$$

in which λ denotes the order of singularity of fundamental solution, and $\overline{f}$ is the nonsingular part of DBIE. We rewrite Eq. (33) using linear integral around the edge of element, i.e.

$$I^e(X) = \int_L \frac{1}{\rho(\mathbf{x},\mathbf{y})} \frac{\partial \rho(\mathbf{x},\mathbf{y})}{\partial \mathbf{n}_L} F(\mathbf{x},\mathbf{y}) dL \tag{35}$$

where $\mathbf{n}_L$ is the outer normal vector of square sides, and

$$F(\mathbf{x},\mathbf{y}) = \lim_{\rho_\alpha(\varepsilon)\to 0} \int_{\rho_\alpha(\varepsilon)}^{\rho(\mathbf{x},\mathbf{y})} \frac{\overline{f}(\boldsymbol{\chi},\mathbf{x})}{r^{\lambda}(\boldsymbol{\chi},\mathbf{x})} J_e \rho d\rho \tag{36}$$

in which ρ is the distance in parametric space between source point $\mathbf{x}$ and selected point χ, and it is defined as

$$\rho = \sqrt{(\xi-\xi_p)^2 + (\eta-\eta_p)^2} \tag{37}$$

Obviously, the local coordinate ξ and η can be represented by ρ,

$$\begin{cases} \xi = \xi_p + \rho\cos\theta \\ \eta = \eta_p + \rho\sin\theta \end{cases} \tag{38}$$

In order to degenerate the singularity, we reformulate the distance by radius expansion as

$$\frac{r}{\rho} = (\sum_{m=0}^{M} G_m \rho^m)^{1/2} = \sum_{n=0}^{N} C_n \rho^n \tag{39}$$

where (M -1) is the total number of interpolation points between $\mathbf{x}$ and $\mathbf{y}$, and G_m can be obtained from Eq. (39)

$$\mathbf{R}(M)\mathbf{G} = \mathbf{Z} \tag{40}$$

in which

$$\begin{aligned} Z_m &= [(r_m/\rho_m)^2 - G_0]/\rho_m, \\ R_m &= [1\ \rho_m \cdots \rho_m^{M-1}], \end{aligned} \qquad m = 1, 2, \ldots, M \tag{41}$$

and

$$G_0 = \lim_{\rho\to 0}(\frac{r}{\rho})^2 = \left|\frac{\partial \mathbf{r}}{\partial \xi}\rho_{,\xi} + \frac{\partial \mathbf{r}}{\partial \eta}\rho_{,\eta}\right| \tag{42}$$

The number of interpolation points M is shown as Table 1, and more details can be found in [45].

We derive the radius integral by power series form of ρ, which is expressed as

$$F(\mathbf{x}, \mathbf{y}) = \sum_{k=0}^{K} B^{(k)} \lim_{\rho_\alpha(\varepsilon)\to 0} \int_{\rho_\alpha(\varepsilon)}^{\rho(\mathbf{x},\mathbf{y})} \rho^{k-\lambda+1} d\rho = \sum_{k=0}^{K} B^{(k)} E_k \tag{43}$$

where

$$E_k = \begin{cases} \dfrac{1}{k-\lambda+2}[\dfrac{1}{\rho^{\lambda-k-2}(X,Y)} - \lim\limits_{\rho_\alpha(\varepsilon)\to 0} \dfrac{1}{\rho_\alpha^{\lambda-k-2}(\varepsilon)}], & k \neq \lambda - 2 \\ \ln\rho(X,Y) - \lim\limits_{\rho_\alpha(\varepsilon)\to 0} \ln\rho_\alpha(\varepsilon), & k = \lambda - 2 \end{cases} \tag{44}$$

Extracting the limiting part from finite part of Eq. (44), which can be reformulated to the sum of finite and infinite parts as

$$\begin{cases} \lim\limits_{\rho_s\to 0} \ln\rho_s(\varepsilon) = \ln H_0 + \infty, \\ \lim\limits_{\rho_s\to 0} \dfrac{1}{\rho_s^{\lambda-k-1}(\varepsilon)} = H_{\lambda-k-1} + \infty, \quad 0 \le k \le \lambda - 2 \end{cases} \tag{45}$$

where

$$\begin{cases} H_0 = 1/C_0;\ H_1 = \overline{C}_1;\ H_2 = 2\overline{C}_2 - \overline{C}_1^2 \\ H_3 = 3\overline{C}_3 - 3\overline{C}_1\overline{C}_2 + \overline{C}_1^2; \\ H_4 = 4\overline{C}_4 + 4\overline{C}_1^2\overline{C}_2 - 4\overline{C}_1\overline{C}_2 - 2\overline{C}_2^2 - \overline{C}_1^4 \end{cases} \tag{46}$$

in which $\overline{C}_i = C_i/C_0$.

There are definite results of numerical integrals for a practical physical problem. In other words, the infinitesimal part of Eq. (44) tends to zero when the radius distance approaches zero, Eq. (44) can be rewritten as

$$E_k = \begin{cases} \dfrac{1}{k-\lambda+2}[\dfrac{1}{\rho^{\lambda-k-2}(X,Y)} - H_{\lambda-k-2}], & 0 \le k \le \lambda - 3 \\ \ln\rho(X,Y) - \ln H_0, & k = \lambda - 2 \\ \dfrac{\rho^{k-\lambda+2}(X,Y)}{k-\lambda+2}, & k > \lambda - 2 \end{cases} \tag{47}$$

For hypersingular integral in 2D problems, the singular order λ is up to 5. Meanwhile, this power series expansion method can be used to solve hypersingular integral whose order is up to 6 in 3D problems.

Table 1
The values of the power M.

N_{node}	4	8	9
M	2	4	6

4. IGABEM for shape sensitivity and optimization analysis

4.1. IGABEM shape sensitivity analysis

Shape sensitivity refers to the calculation of sensitivity to the objective functions and constraints. It is a key step for gradient-based optimization analysis and is often used to verify the accuracy and efficiency of numerical algorithms. In the process of isogeometric shape optimization, the control points and weights have been chosen as the design variables to approximate objective shape. However, it is more convenient and common to carry out optimization analysis only by control points. The implicit differentiation method applies the derivative of the design variable on the boundary and obtains the expression of the shape sensitivity of DBIE.

The implicit differential method is used to derive the boundary integral equation, and Eq. (19) is converted to

$$\begin{aligned}\dot{\mathbf{C}}(\mathbf{x})\mathbf{u}(\mathbf{x}) + \mathbf{C}(\mathbf{x})\dot{\mathbf{u}}(\mathbf{x}) = B\dot{\mathbf{u}^{\mathbf{0}}}(\mathbf{x}) &+ \int_S [\dot{\mathbf{U}}(\mathbf{x},\mathbf{y})\mathbf{t}(\mathbf{y}) + \mathbf{U}(\mathbf{x},\mathbf{y})\dot{\mathbf{t}}(\mathbf{y})]dS \\ &- \int_S [\dot{\mathbf{T}}(\mathbf{x},\mathbf{y})\mathbf{u}(\mathbf{y}) + \mathbf{T}(\mathbf{x},\mathbf{y})\dot{\mathbf{u}}(\mathbf{y})]dS \\ &+ \int_S [\mathbf{U}(\mathbf{x},\mathbf{y})\mathbf{t}(\mathbf{y}) - \mathbf{T}(\mathbf{x},\mathbf{y})\mathbf{u}(\mathbf{y})]d\dot{S}\end{aligned} \tag{48}$$

where $(\cdot)$ denotes the derivative of functions with respect to design variables, $\dot{\mathbf{C}}(\mathbf{x})$ is the derivative of coefficient matrix $\mathbf{C}(\mathbf{x})$, and it is cumbersome to calculate this special coefficient matrix. However, we can remove the value of that $\dot{C}(\mathbf{x})$ using the improved Greville abscissae method. Thus, the shape sensitivity of DBIE in Eq. (48) can be reformulated as

$$\begin{aligned}\frac{1}{2}\dot{\mathbf{u}}(\mathbf{x}) = B\dot{\mathbf{u}^{\mathbf{0}}}(\mathbf{x}) &+ \int_S [\dot{\mathbf{U}}(\mathbf{x},\mathbf{y})\mathbf{t}(\mathbf{y}) + \mathbf{U}(\mathbf{x},\mathbf{y})\dot{\mathbf{t}}(\mathbf{y})]dS \\ &- \int_S [\dot{\mathbf{T}}(\mathbf{x},\mathbf{y})\mathbf{u}(\mathbf{y}) + \mathbf{T}(\mathbf{x},\mathbf{y})\dot{\mathbf{u}}(\mathbf{y})]dS \\ &+ \int_S [\mathbf{U}(\mathbf{x},\mathbf{y})\mathbf{t}(\mathbf{y}) - \mathbf{T}(\mathbf{x},\mathbf{y})\mathbf{u}(\mathbf{y})]d\dot{S}\end{aligned} \tag{49}$$

The shape sensitivities of kernel functions in 2D problems corresponding to design variables are as follows

$$\dot{U}_{ij} = \frac{1}{8\pi\mu(1-\upsilon)}[(3-4\upsilon)(\ln\dot{\frac{1}{r}})\delta_{ij} + (\dot{r_{,i}})r_{,j} + r_{,i}(\dot{r_{,j}})] \tag{50}$$

$$\begin{aligned}\dot{T_{ij}} = &\frac{-1}{4\pi(1-\upsilon)}(\frac{\dot{1}}{r})\left\{\frac{\partial r}{\partial n}[(1-2\upsilon)\delta_{ij} + 2r_{,i}r_{,j}]\right\} \\ &\frac{-1}{4\pi(1-\upsilon)}(\frac{\dot{1}}{r})[-(1-2\upsilon)(r_{,i}n_j - r_{,j}n_i)] \\ &\frac{-1}{4\pi(1-\upsilon)r}\left\{(\frac{\dot{\partial r}}{\partial n})[(1-2\upsilon)\delta_{ij} + 2r_{,i}r_{,j}] + 2\frac{\partial r}{\partial n}[(\dot{r_{,i}})r_{,j} + r_{,i}(\dot{r_{,j}})]\right. \\ &\left.-(1-2\upsilon)[(\dot{r_{,i}})n_j + r_{,i}\dot{n_j} - (\dot{r_{,j}})n_i - r_{,j}\dot{n_i}]\right\}\end{aligned} \tag{51}$$

and the shape sensitivities of kernel functions in 3D problems corresponding to design variables are as follows

$$\dot{U}_{ij} = \frac{1}{16\pi\mu(1-\upsilon)}\left\{(\frac{\dot{1}}{r})[(3-4\upsilon)\delta_{ij} + r_{,i}r_{,j}] + \frac{1}{r}[(\dot{r}_{,i})r_{,j} + r_{,i}(\dot{r}_{,j})]\right\} \tag{52}$$

$$\begin{aligned}\dot{T_{ij}} = &\frac{-1}{8\pi(1-v)}(\frac{\dot{1}}{r^2})\left\{\frac{\partial r}{\partial n}[(1-2v)\delta_{ij}+3r_{,i}r_{,j}]+(1-2v)(n_i r_{,j}-n_j r_{,i})\right\}\\ &+\frac{-1}{8\pi(1-v)r^2}\left\{(\frac{\partial\dot{r}}{\partial n})[(1-2v)\delta_{ij}+3r_{,i}r_{,j}]+3\frac{\partial r}{\partial n}[(\dot{r_{,i}})r_{,j}+r_{,i}(\dot{r_{,j}})]\right\}\\ &+\frac{-1}{8\pi(1-v)r^2}\{(1-2v)[\dot{n_i}r_{,j}+n_i(\dot{r_{,j}})-\dot{n_j}r_{,i}-n_j(\dot{r_{,i}})]\}\end{aligned} \tag{53}$$

where the singular orders of the sensitivities of fundamental solutions can be demonstrated from Appendix A. There are some basic parameters in the above four sensitivities of kernel functions, which can be expressed as

$$(\frac{\partial\dot{r}}{\partial n}) = (r_{,i}\dot{n}_i) = (\dot{r_{,i}})n_i + r_{,i}\dot{n_i}, \quad (\frac{\dot{1}}{r}) = -\frac{\dot{r}}{r^2} \tag{54}$$

$$(\dot{r_{,i}}) = (\frac{x_i \dot{-} s_i}{r}) = \frac{(\dot{x_i}-\dot{s_i})r-(x_i-s_i)\dot{r}}{r^2}, \quad (\ln\frac{\dot{1}}{r}) = -\frac{\dot{r}}{r} \tag{55}$$

$$\dot{r} = \left[\sqrt{(x_i-s_i)(x_i-s_i)}\right] = \frac{(\dot{x_i}-\dot{s_i})(x_i-s_i)}{r} \tag{56}$$

$$\dot{n_i}(\mathbf{s}) = \left[\frac{J_i(\mathbf{s})}{J(\mathbf{s})}\right] = \frac{\dot{J_i}(\mathbf{s})J(\mathbf{s})-J_i(\mathbf{s})\dot{J}(\mathbf{s})}{J^2(\mathbf{s})} \tag{57}$$

in which the Jacobian is $J(\mathbf{s}) = \sqrt{J_i(\mathbf{s})J_i(\mathbf{s})}$, and the shape derivative of Jacobian is given as $\dot{J}(\mathbf{s}) = [\dot{J_i}(\mathbf{s})J_i(\mathbf{s})]/J(\mathbf{s})$. It is worthy noticing that the repetition of subscripts implies a summation of variables. There are many other kernel functions and their shape sensitivities for elastic problems in [29].

When the control points are chosen as design variables, we can derive the shape sensitivity of coordinates about each collocation point on edge, and the expression corresponding to Eq. (12) is as follows

$$\dot{\mathbf{x}}(\mathbf{s}) = \sum_{A=1}^{N_A} R_A(\mathbf{s})\dot{\mathbf{P}}_A \tag{58}$$

which are evaluated from three types of control points as follows:

- Independent control points. For control points are chosen as design variables, the associated shape derivatives are unity when the global index of control points are equal to A, and zero for otherwise.
- Fixed control points. Some control points are fixed in shape optimization procedure, and their shape derivatives are always zero.
- Coupled control points. To keep optimized geometry "reasonably", some control points which are not the design variables, also need to move according to some rules, and their shape derivatives are also acquired from those rules directly.

Similarly, the other variables' sensitivities are also expressed by $\dot{P}_A$ according to implicit differentiation method, such as

$$\dot{r} = |\mathbf{x} \dot{-} \mathbf{y}| = \left|\sum_{A=1}^{N_A}[R_A(\mathbf{s}_p)-R_A(\mathbf{s}_q)]\dot{\mathbf{P}}_A\right| \tag{59}$$

Meanwhile, the shape sensitivities of displacement and traction vectors can be descripted by NURBS basis functions as

$$\dot{\mathbf{u}}(\mathbf{s}) = \sum_{A=1}^{N_A} R_A(\mathbf{s})\dot{\tilde{\mathbf{u}}}_A \tag{60}$$

$$\dot{\mathbf{t}}(\mathbf{s}) = \sum_{A=1}^{N_A} R_A(\mathbf{s})\dot{\tilde{\mathbf{t}}}_A \tag{61}$$

Discretizing the shape sensitivity of boundary integral equation, Eq. (49) can be reformulated as

$$\begin{aligned}\frac{1}{2}\sum_{\alpha=1}^{N} R_{\alpha}^{\bar{e}}(\mathbf{s}_p)\dot{\tilde{u}}_j^{\bar{e}\alpha} = B\dot{u}^0(\mathbf{s}_p) &+ \sum_{e=1}^{E}\sum_{\alpha=1}^{N}\int_{\mathbf{s}_e}[\dot{U}_{ij}(\mathbf{x}(\mathbf{s}_p),\mathbf{y}(\mathbf{s}_q))R_{\alpha}^{e}(\mathbf{s}_q)\tilde{t}_j^{e\alpha}\\ &+ U_{ij}(\mathbf{x}(\mathbf{s}_p),\mathbf{y}(\mathbf{s}_q))R_{\alpha}^{e}(\mathbf{s}_q)\dot{t}_j^{e\alpha}]J\,d\mathbf{s}_e\\ &- \sum_{e=1}^{E}\sum_{\alpha=1}^{N}\int_{\mathbf{s}_e}[\dot{T}_{ij}(\mathbf{x}(\mathbf{s}_p),\mathbf{y}(\mathbf{s}_q))R_{\alpha}^{e}(\mathbf{s}_q)\tilde{u}_j^{e\alpha}\\ &+ T_{ij}(\mathbf{x}(\mathbf{s}_p),\mathbf{y}(\mathbf{s}_q))R_{\alpha}^{e}(\mathbf{s}_q)\dot{\tilde{u}}_j^{e\alpha}]J\,d\mathbf{s}_e\\ &+ \sum_{e=1}^{E}\sum_{\alpha=1}^{N}\int_{\mathbf{s}_e}[U(\mathbf{x}(\mathbf{s}_p),\mathbf{y}(\mathbf{s}_q))R_{\alpha}^{e}(\mathbf{s}_q)\tilde{t}_j^{e\alpha}\\ &- T(\mathbf{x}(\mathbf{s}_p),\mathbf{y}(\mathbf{s}_q))R_{\alpha}^{e}(\mathbf{s}_q)\tilde{u}_j^{e\alpha}]\dot{J}\,d\mathbf{s}_e\end{aligned} \tag{62}$$

All the equations of all collocation points from the improved Greville abscissae method are collected, and a system of linear equations based on Eq. (62) is obtained as follows:

$$\mathbf{H}\dot{\tilde{\mathbf{u}}} + \dot{\mathbf{H}}\tilde{\mathbf{u}} = B\dot{\mathbf{u}}^0 + \mathbf{G}\dot{\tilde{\mathbf{t}}} + \dot{\mathbf{G}}\tilde{\mathbf{t}} \tag{63}$$

Meanwhile, the sensitivity of unknown fields at particular control points can be obtained from the following equations

$$\begin{cases}\mathbf{H}_1\dot{\tilde{\mathbf{u}}}_1 + \dot{\mathbf{H}}_1\tilde{\mathbf{u}}_1 = B\dot{\mathbf{u}}^0 + \mathbf{G}_1\dot{\tilde{\mathbf{t}}}_1 + \dot{\mathbf{G}}_1\tilde{\mathbf{t}}_1\\ \mathbf{H}_2\dot{\tilde{\mathbf{u}}}_2 + \dot{\mathbf{H}}_2\tilde{\mathbf{u}}_2 = \mathbf{G}_2\dot{\tilde{\mathbf{t}}}_2 + \dot{\mathbf{G}}_2\tilde{\mathbf{t}}_2\end{cases} \tag{64}$$

in which the displacement vector $\tilde{\mathbf{u}}$ and traction vector $\tilde{\mathbf{t}}$ on control points are the same as those in Eq. (32), and the sensitivities of those values also satisfy displacement continuous and traction balance conditions, i.e. $\dot{\tilde{\mathbf{u}}}_1 = \dot{\tilde{\mathbf{u}}}_2, \dot{\tilde{\mathbf{t}}}_1 = -\dot{\tilde{\mathbf{t}}}_2$. It is worth noting that the global index of coefficient matrices $\dot{\mathbf{H}}_2$ and $\dot{\mathbf{G}}_2$ must be converted, as in Eq. (32). Meanwhile, Eq. (64) can be assembled as an algebraic system with the same method as Eq. (32),

$$\begin{bmatrix}\mathbf{H}_1 & \dot{\mathbf{H}}_1\\ \mathbf{H}_2 & \dot{\mathbf{H}}_2\end{bmatrix}\begin{bmatrix}\dot{\tilde{\mathbf{u}}}_1 & \tilde{\mathbf{u}}_1\end{bmatrix} = \begin{bmatrix}\mathbf{B}\\ \mathbf{0}\end{bmatrix}\begin{bmatrix}\dot{\mathbf{u}}^0\end{bmatrix} + \begin{bmatrix}\mathbf{G}_1 & \dot{\mathbf{G}}_1\\ -\mathbf{G}_2 & -\dot{\mathbf{G}}_2\end{bmatrix}\begin{bmatrix}\dot{\tilde{\mathbf{t}}}_1 & \tilde{\mathbf{t}}_1\end{bmatrix} \tag{65}$$

4.2. Sensitivity propagation from the design model to the analysis model

Isogeometric analysis with NURBS, T-splines, PHT-splines can be used to accurately model the geometries in CAD software. However, the accuracy of solutions, which is approximated by collocation point or Galerkin method, is not as high as that of geometry. In order to acquire higher accuracy of solution, the geometry mesh should be refined by *h*-, *p*-, or *k*-refinement. After that, we can do the same things in shape optimization process to get the sensitivity propagation from the design model to analysis model.

We focus on the application of sensitivity propagation during *h*-refinement, and only some conclusions are given. Sensitivity propagation formulations for other refinements can be derived similarly and acquired from [10].

If we insert a new knot $\xi' \in [\xi_k, \xi_{k+1}]$, the added point P' can be obtained as follows without changing the geometry:

$$P'_A = \begin{cases}P_1 & A = 1\\ \alpha_A P_A + (1-\alpha_A)P_{A-1} & 1 < A < n\\ P_n & A = n\end{cases} \tag{66}$$

with

$$\alpha_A = \begin{cases}1 & 1 \le A \le k-p\\ \dfrac{\xi'_A - \xi_A}{\xi_{A+p} - \xi_A} & k-p+1 \le A \le k\\ 0 & A \ge k+1\end{cases} \tag{67}$$

Thus, the position of the new control point's projection in 2D becomes that:

$$P'_A = \frac{\alpha_A P_A + (1-\alpha_A)P_{A-1}}{\alpha_A w_A + (1-\alpha_A)w_{A-1}} \tag{68}$$

From Eq. (68), the new sensitivity about point and weight can be given as

$$\begin{aligned}\dot{P}'_A = &\frac{(1-\alpha_A)(\dot{P_{A-1}}w_{A-1} + P_{A-1}\dot{w_{A-1}}) + \alpha_A(\dot{P}_A w_A + P_A \dot{w}_A)}{\alpha_A w_A + (1-\alpha_A)w_{A-1}} \\ &- \frac{(1-\alpha_A)P_{A-1}w_{A-1} + \alpha_A P_A w_A}{(\alpha_A w_A + (1-\alpha_A)w_{A-1})^2}(\alpha_A \dot{w}_A + (1-\alpha_A)\dot{w_{A-1}})\end{aligned} \tag{69}$$

By repeating the above knot insertion procedure and the sensitivity propagation to all rows and columns of control points, we can get the dense mesh and sensitivity propagation in a surface of 3D problems.

4.3. Shape optimization analysis with IGABEM

Shape optimization can be conducted through a gradient-free or gradient-based method. The gradient-free method, i.e. genetic algorithm (GA) [57], multi-island genetic algorithm (MIGA) [58], adaptive simulated annealing (ASA) [59], does not require for shape derivatives information, but can be unreasonable time-consuming for realistic problems and its optimization results are not associated with initial results. So, the gradient-based method, i.e. the method of moving asymptotes (MMA) [29], sequential quadratic programming (SQP) [60], is commonly used in IGA for shape optimization process.

In this section, the shape optimization analysis based on gradient-based optimization method (MMA) is applied to elastic problems based on IGABEM, and its basic structure is as follows

$$\begin{cases} \min\ \Phi(\mathbf{t}) \rightarrow \max\ \{-\Phi(\mathbf{t})\} \\ s.t.\ g_i(\mathbf{t}) \le 0,\ 1 \le i \le N \\ \quad \mathbf{t}^{\min} \le \mathbf{t} \le \mathbf{t}^{\max} \end{cases} \tag{70}$$

The traditional MMA algorithm aims to find the minimum value of objective function $\Phi(\mathbf{t})$ subjected to constraints $g_i(\mathbf{t})$, in which $\mathbf{t}$ means the design variable vector between minimum and maximum values. Here, we derive minus value of objective functions to obtain maximum value. The volume or area of structure can be calculated as

$$V = \int_\Omega d\Omega = \frac{1}{\beta}\int_\Omega \nabla \cdot \mathbf{x} d\Omega = \frac{1}{\beta}\int_S \mathbf{x}\cdot\mathbf{n} dS \tag{71}$$

where β denotes the dimension of problem.

The shape sensitivity of volume constraint is formulated as

$$\dot{V} = \frac{1}{\beta}\int_S \dot{\mathbf{x}}\cdot\mathbf{n} dS + \mathbf{x}\cdot\dot{\mathbf{n}} dS + \mathbf{x}\cdot\mathbf{n} d\dot{S} \tag{72}$$

We use the iterative method to obtain objective value until numerical result converges, the procedure about shape optimization of heterogeneous structure is illustrated in Fig. 5.

5. Numerical examples

In this section, numerical examples are used to verify the accuracy and efficiency of the present method and run on a single processor computer Inter® Core™ i7-8550U CPU @ 1.8 GHz using Fortran 95 with OpenMP parallelization. The objective function Φ is chosen as elastic energy increment of composite materials, which is formulated as [61]

$$\Delta U = \frac{1}{2}\int_S \left[\left(1 - \frac{(1+\nu_1)E_2}{(1+\nu_2)E_1}\right)t_i^0 - \frac{(\nu_2-\nu_1)(1+\nu_1)E_2}{(1+\nu_2)(1-2\nu_2)E_1}\sigma_{mm}^0 n_i\right] u_i dS \tag{73}$$

where ν and E are the Poisson's ratio and elastic modulus, the subscripts 1 and 2 are material identification numbers as shown in Fig. 3(a), the superscript 0 denotes the values deriving from remote boundary conditions, and σ is stress. u_i and t_i ($i = 1, 2, 3$ for 3D problem) are, respectively, the ith displacement and ith traction components over the

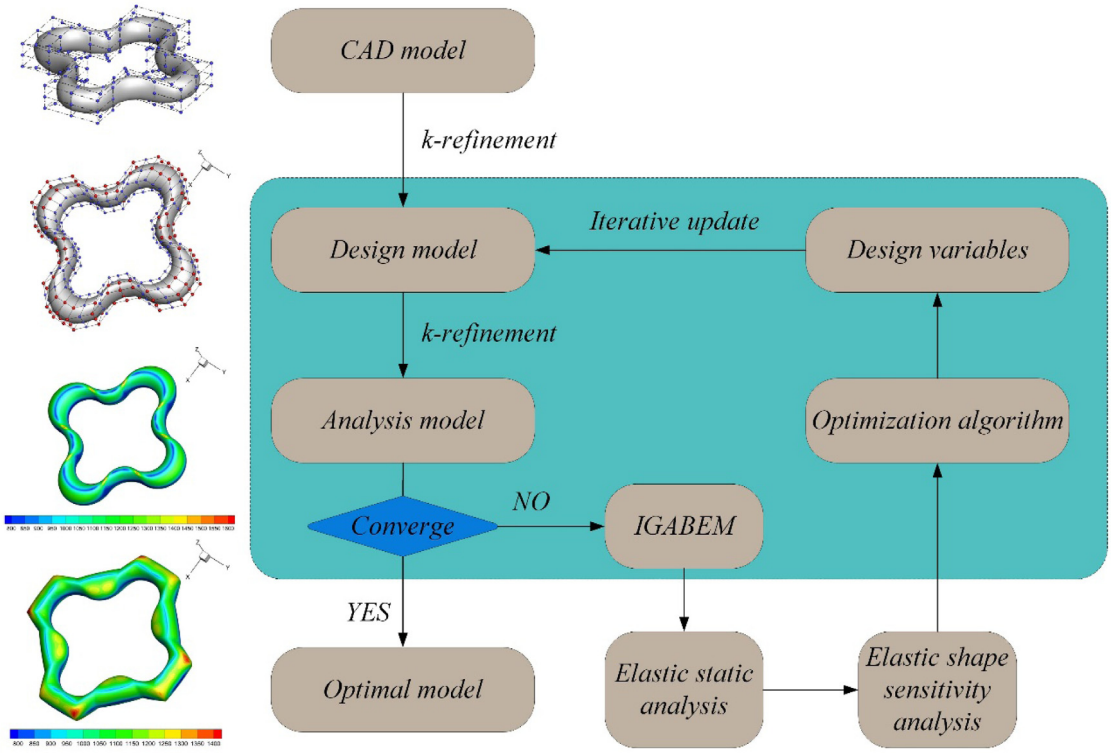

Fig. 5. Flowchart of the shape optimization of heterogeneous structure in IGABEM.

interface S. The repeated indexes imply summation. n_i denotes the ith direction cosine of unit vector $\mathbf{n}$ relative to the existing coordinate system. The objective of shape optimization is to maximize elastic energy increment of heterogeneous structure. To carry out the convergence and error analysis, the relative error is defined as

$$\varepsilon_r = \left| \frac{I_{num} - I_{ref}}{I_{ref}} \right| \tag{74}$$

in which I_{num} and I_{ref} denote numerical and analytical results, respectively.

5.1. 2D inclusion models

5.1.1. Circular inclusion model

Consider one circular inclusion model (see Fig. 6) with radius $r=3$ m, embedded into an infinite matrix and subjected to remote traction boundary condition $\sigma_1^0 = \sigma_2^0 = \sigma^0 = 10^4$. The material parameters are Young's modulus $E_1 = 10^4$, $E_2 = 2\times 10^4$ and Poisson's ratio $v_1 = 0.3$, $v_2 = 0.2$. The analysis model has 12 control points and 8 elements on the boundary, which is from CAD model by h-refinement with two times. When the radius of circle is chosen as design variable, the shape sensitivities of elastic energy increment and radial displacement can be easily derived from [61] as

$$\dot{\Delta U} = 2\pi\sigma^0 r\dot{u_r}\left(1 - \frac{(1+v_1)E_2}{(1+v_2)E_1} - 2\frac{(v_2-v_1)(1+v_1)E_2}{(1+v_2)(1-2v_2)E_1}\right) \tag{75}$$

where

$$\dot{u_r} = \frac{\sigma^0(1-v_1)}{\mu_1}\left(\frac{1-2v_2}{1-2v_2+\mu_2/\mu_1}\right) \tag{76}$$

in which μ is shear Modulus, and u_r is radial displacement on the interface S.

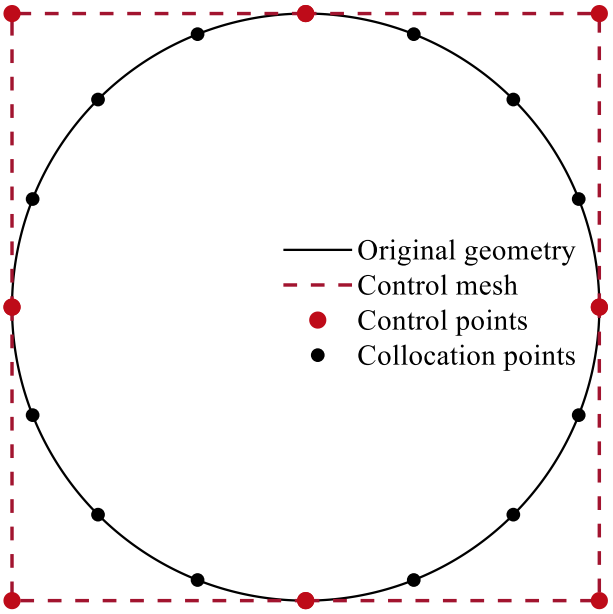

Fig. 6. CAD model: Discretization of circular inclusion model with four NURBS patches. The knot vector is Ξ = {0, 0, 0, 1, 1, 2, 2, 3, 3, 4, 4, 4}. The order of NURBS is p=2 and the weights of control points are $\omega = [1, \frac{\sqrt{2}}{2}, 1, \frac{\sqrt{2}}{2}, 1, \frac{\sqrt{2}}{2}, 1, \frac{\sqrt{2}}{2}, 1]$. The number of control points is 8.

The Subtraction of Singularity Method (SST) and Telles transformation in [50] are used to deal with singular integrals in Eqs. (19) and (48). The comparison between the analytical and the numerical values of the displacements and their sensitivity on collocation points is shown in Fig. 7, and Fig. 8 plots the relative errors of elastic energy increment and its sensitivity in terms of the number of Gauss quadrature points. The error first decreases rapidly and then converges with the increase of Gauss quadrature points. Note that the error evaluations about objective function and its sensitivity analysis have excellent coincidence, which means that shape sensitivity analysis will not substantially increase the existing numerical errors. In order to improve accuracy and efficiency of numerical algorithm, the number of Gauss quadrature points is set to 12, and regular integral to 8. The distribution of Von Mises stress around a circular inclusion model is shown in Fig. 9(a). The result illustrates that the accuracy of IGABEM is better than that of FEM under same amount of degrees of freedom (Dofs). Fig. 9(b) shows that the effect of inclusion will disappear when the distance between the computation point and the center of inclusion is greater than 5r. The conclusion will be of great importance for the computation of infinite domain problems using FEM and some commercial software.

5.1.2. Star inclusion model

One-star inclusion is embedded into an infinite matrix, and the CAD model is descripted by NURBS as shown in Fig. 10, in which the weights of control points are equal to one. The basic material parameters and remote boundary conditions are given in Table 2. The design model is identical with the CAD model, and the radial distance of its control points is taken as design variables. The initial area is 24.6875 and the area constraint is $V \leq 20\pi$ and convergence criteria are *kktnorm*[1] $\leq 10^{-4}$. In the implementation of isogeometric shape optimization, the analysis model is obtained by h-refining the design model twice. The initial values of design variables are obtained from the design model, as shown in Table 3, and the side constraint is $2 \leq \mathbf{t} \leq 5$ for all design variables. Fig. 11 illustrates the convergence of the iteration process, resulting in the optimized geometries as shown in Fig. 12. The final optimized design variables can be seen in Table 3. Through the whole optimization process, the shape optimization for heterogeneous structure can communicate with CAD model without boundary recapture and remeshing, and the potential of the present algorithm in shape optimization for heterogeneous structure is demonstrated.

[1] *kktnorm* denotes the convergence criteria in MMA algorithm.

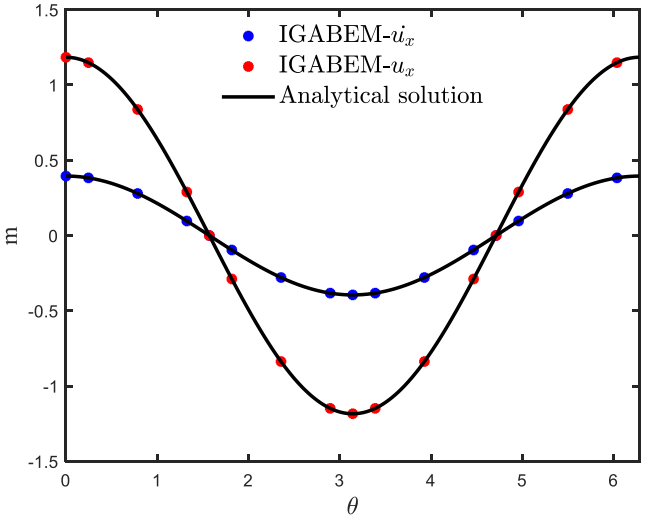

Fig. 7. Displacement sensitivity on x-direction.

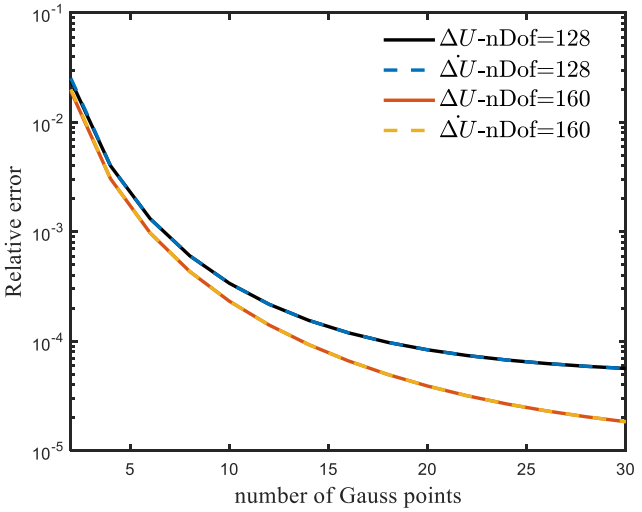

Fig. 8. The relative errors in terms of the number of Gauss quadrature points.

Table 2
Material properties and boundary conditions.

Name	Case I	Case II	Case III	Case IV
E_1	2×10^4	1×10^4	2×10^4	2×10^4
E_2	1×10^4	1×10^4	1×10^4	1×10^4
v_1	0.3	0.3	0.3	0.3
v_2	0.3	0.2	0.3	0.2
σ^0_{xx}	1×10^4	1×10^4	0	1×10^4
σ^0_{yy}	2×10^4	1×10^4	1×10^4	0

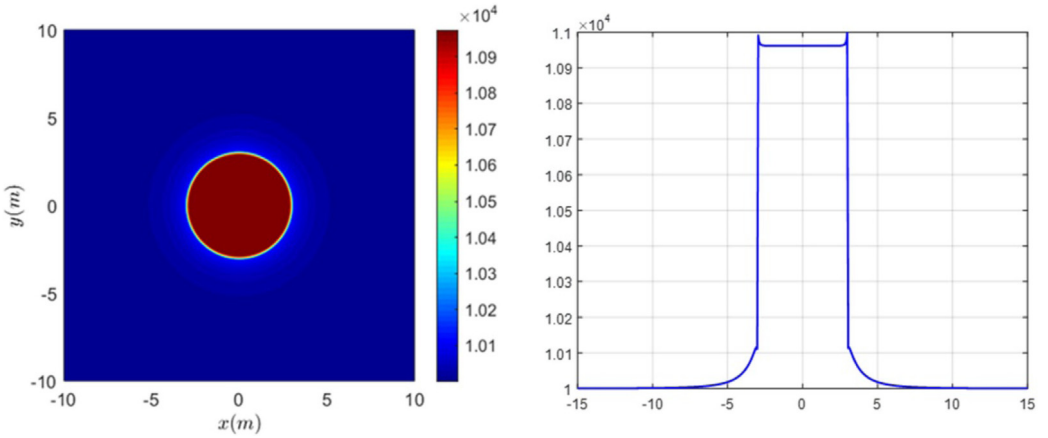

(a) Von Mises stress distribution. (b) The Von Mises stress distribution on x-axis.

Fig. 9. The Von Mises stress distribution.

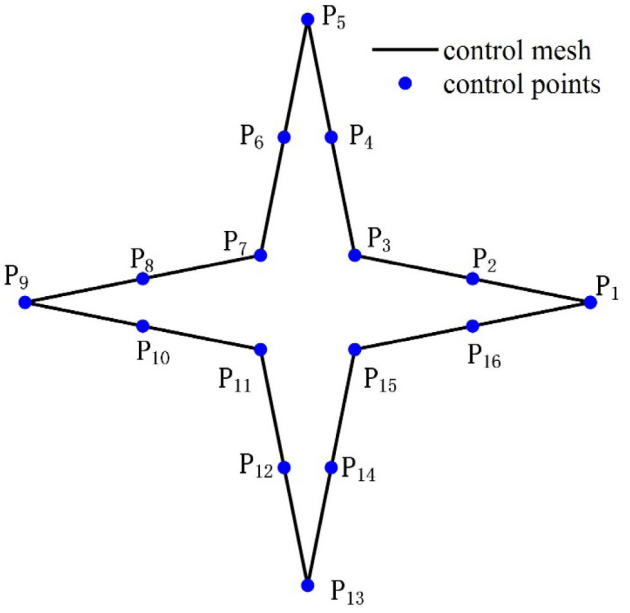

Fig. 10. CAD model: The knot vector is Ξ = {0,0,0,1,2,3,4,5,6,7,8,9,10,11,12,13,14,15,15,15} and the control points are **P** = {(6.0), (3.5,0.5), (1,1), (0.5,3.5), (0,6), (−0.5,3.5), (−1,1), (−3.5,0.5), (−6,0), (−3.5,0.5), (−1,1), (−0.5,−3.5), (0,−6), (0.5,−3.5), (1,−1), (3.5,−0.5), (6,0)}. The degree of NURBS is equal to 2.

5.2. Particle inclusion

In this subsection, the model of a 3D particle inclusion embedded on an infinite matrix is considered to demonstrate the accuracy and effectiveness of the present algorithm. We use the power series expansion method (PSEM) to evaluate the singular integrals in boundary integral equations and their sensitivities.

5.2.1. Sphere model

One spherical inclusion model (see Fig. 13) with radius *r=10.0* m embedded in an infinite matrix can be descripted by bivariable NURBS surface. The remote boundary condition is $\sigma^0_{xx} = \sigma^0_{yy} = \sigma^0_{zz} = \sigma^0 = 10^3$, and the material parameters of the heterogeneous structure are given in Fig. 13. Meanwhile, in order to facilitate error

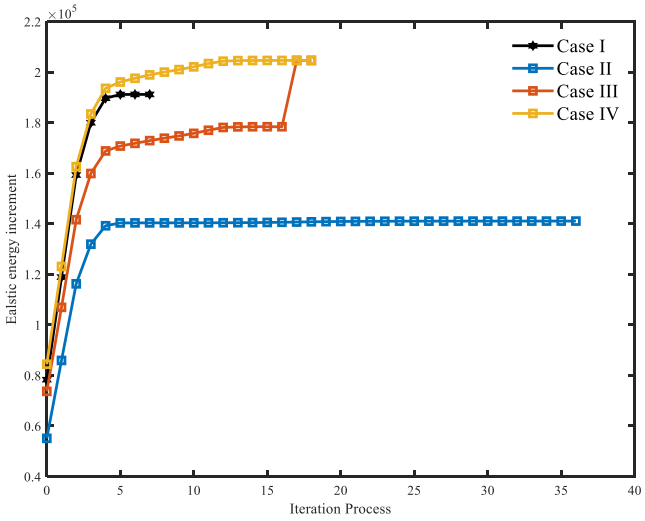

Fig. 11. Objective functions in terms of iteration step.

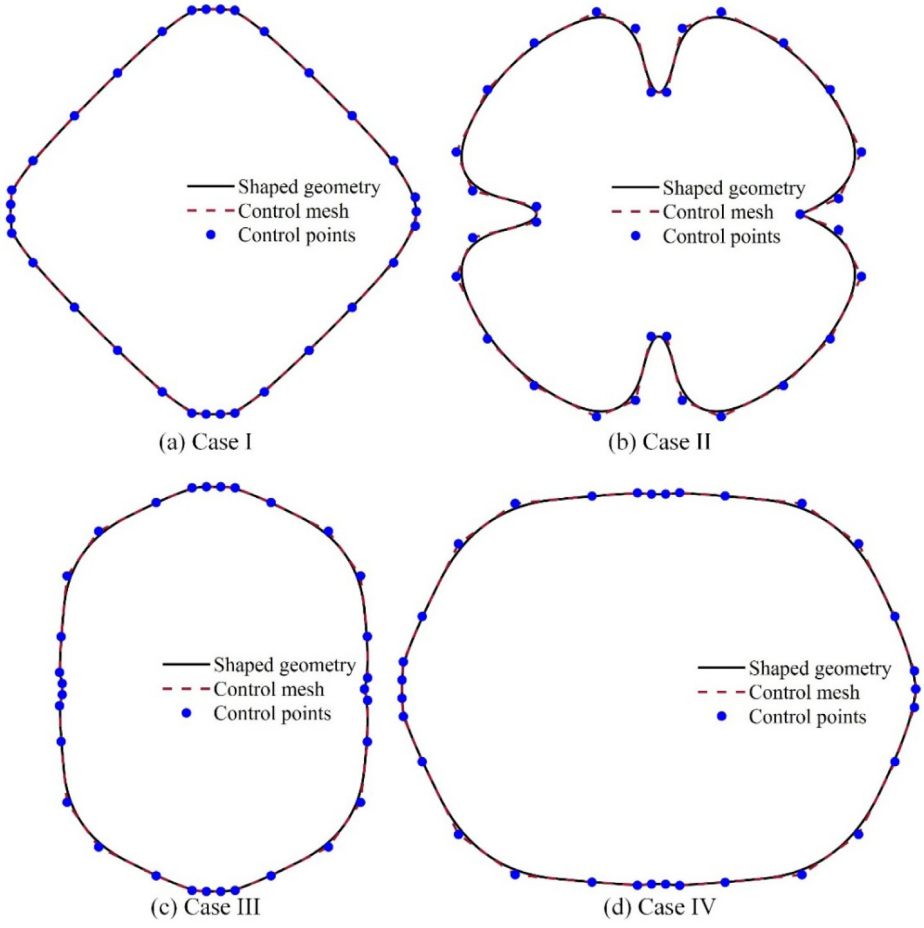

Fig. 12. The optimized geometries for star inclusion.

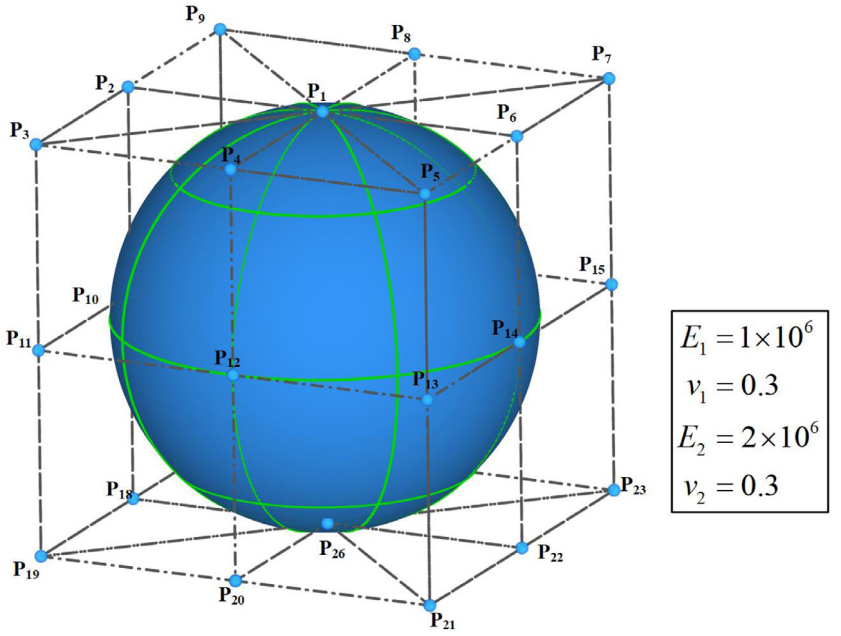

Fig. 13. CAD model: The two knot vectors for NURBS surface are Ξ = {0, 0, 0, 1, 1, 2, 2, 3, 3, 4, 4, 4} and $\Re$ = {0, 0, 0, 1, 1, 2, 2, 2}. Degree 2 is chosen in both directions. This NURBS surface can be divided into 8 patches by continuity of knot vectors. The numbers of elements and control points are 8 and 26, respectively. The coordinates of control points are (0, 0, 10) for P_1, (10, 10, 0) for P_{11} and (0, 0, −10) for P_{26}.

Table 3
Design variables in single 2D inhomogeneity.

Index	Initial value	Lower bound	Upper bound	Final value			
				Case I	Case II	Case III	Case IV
1	6.0000	2	5	5.0000	3.2052	3.7142	5.0000
2	3.5355	2	5	5.0000	5.0000	3.9089	5.0000
3	1.4142	2	5	4.1169	5.0000	5.0000	5.0000
4	3.5355	2	5	5.0000	5.0000	5.0000	3.8727
5	6.0000	2	5	5.0000	2.0451	5.0000	3.7830
6	3.5355	2	5	5.0000	5.0000	5.0000	3.8682
7	1.4142	2	5	4.1111	5.0000	5.0000	5.0000
8	3.5355	2	5	5.0000	5.0000	3.8646	5.0000
9	6.0000	2	5	5.0000	2.0531	3.6925	5.0000
10	3.5355	2	5	5.0000	5.0000	3.8646	5.0000
11	1.4142	2	5	4.1111	5.0000	5.0000	5.0000
12	3.5355	2	5	5.0000	5.0000	5.0000	3.8682
13	6.0000	2	5	5.0000	2.0451	5.0000	3.7830
14	3.5355	2	5	5.0000	5.0000	5.0000	3.8727
15	1.4142	2	5	4.1169	5.0000	5.0000	5.0000
16	3.5355	2	5	5.0000	5.0000	3.9089	5.0000

evaluation, the radius r of the sphere model is set as design variable. Therefore, the shape sensitivity of elastic energy increment and radial displacement are formulated as follows [61]:

$$\dot{\Delta U} = 6\pi r^2 \sigma^0 \dot{u_r}(1 - \frac{(1+v_1)E_2}{(1+v_2)E_1} - 3\frac{(v_2 - v_1)(1+v_1)E_2}{(1+v_2)(1-2v_2)E_1}) \tag{77}$$

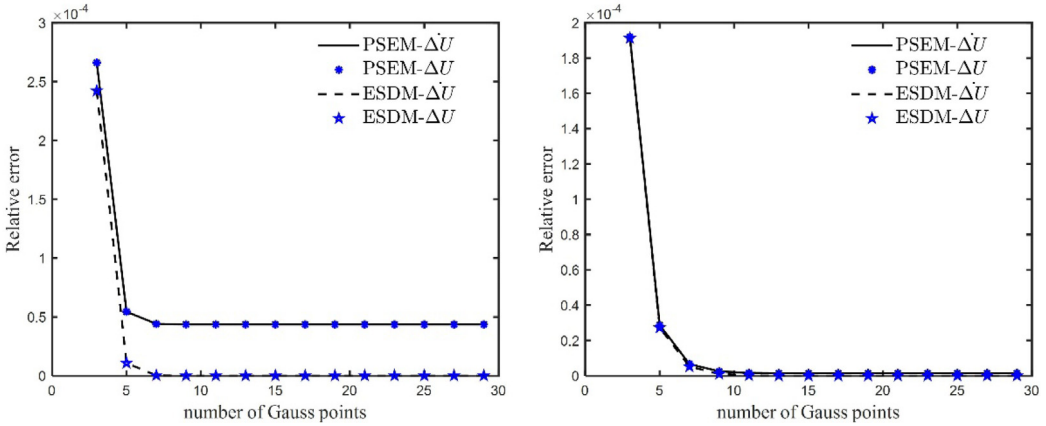

Fig. 14. The comparison of relative error between PSEM and ESDM. The numbers of degrees of freedom are obtained from different h-refinement meshes, for example, when refinement time is equal to 0 or 1, the Dof is equal to 312 or 1368. The coordinates on x-axis mean the number of Gauss points, i.e. 8 in x-axis denotes 8×8 Gauss points.

and

$$\dot{u_r} = \frac{1.5\sigma^0(1-v_1)(1-2v_2)}{0.5(1+v_1)E_2+(1-2v_2)E_1} \tag{78}$$

In the process of isogeometric shape optimization based on BEM, the element sub-division method (ESDM) based on the regularized boundary integral equation [29] is the common method to avoid corner point problem as mentioned before. Here, the simple explanation of this method is given in Appendix B. Fig. 14 gives the comparison between PSEM and ESDM about the values of elastic energy increment and its sensitivity in terms of the number of Gauss quadrature points for singular integrals, in which the number of Gauss quadrature points for regular integrals is equal to 20. The error first decreases rapidly and then converges with the increase of Gauss quadrature points. Note that the relative errors of elastic energy have excellent consistence with their sensitivities whether they come from PSEM or ESDM. In order to improve accuracy and efficiency, in the following 3D example, 8×8 Gauss points are selected for regular integration, and 11×11 Gauss points are selected for singular integration. To give a fair comparison of CPU time, only the integration computation part is compared because all the other costs are the same between the PSEM and the ESDM. In Fig. 15, the relative error about sensitivity of elastic energy increment decreases as the Dofs increase. However, the PSEM shows more consistent and convergence than the ESDM. Meanwhile, the CPU-time of the ESDM will exceed that of the PSEM as the Dofs increase. The result shows that the PSEM owns more accuracy and efficiency than the ESDM under the same number of Gauss quadrature points and Dofs.

5.2.2. Spherical inclusion

The spherical inclusion can help us to investigate the shape optimization of heterogeneous structure in infinite domain. Note that this test case has been implemented in [62,63] to deal with isogeometric shape optimization for thin structures with a solid-shell. For simplicity, the symmetry of geometry allows to consider one eighth of sphere. Once the initial mesh of CAD model is built as shown in Fig. 13, the design model as shown in Fig. 16 can be acquired by h-refining CAD model twice. In order to acquire smooth and comfortable geometry shape after iterative optimization, the radial distances of sixteen control points which locate on C^1-continuous boundary are chosen as design variables. And the coupled control points maintain an initial geometric relationship with the corresponding design variables (see Fig. 16), that is, only the distance between the design variables and the center of the sphere changes during iteration. The optimization objective is to obtain maximum elastic energy increment of heterogeneous structure. The material parameters can be obtained in Fig. 16. The initial volume is 4188.79 and the volume constraint is $V \leq 4188.79$ and the convergence criteria are $kktnorm \leq 10^{-4}$. The initial values of control points and the side constraints can be seen in Table 4. Here, to verify the robustness of the present method, two remoting stress fields are considered, i.e.

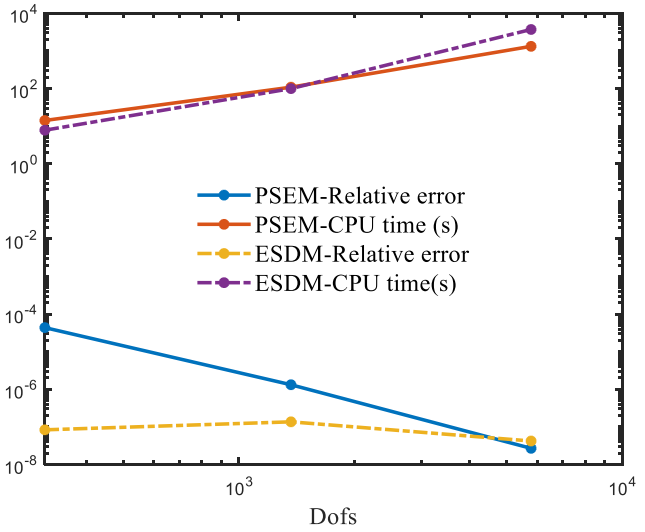

Fig. 15. The comparison about relative error and CPU time between PSEM and ESDM. The Dofs mean the number of degrees of freedom, and it can be obtained from different *h*-refinement levels.

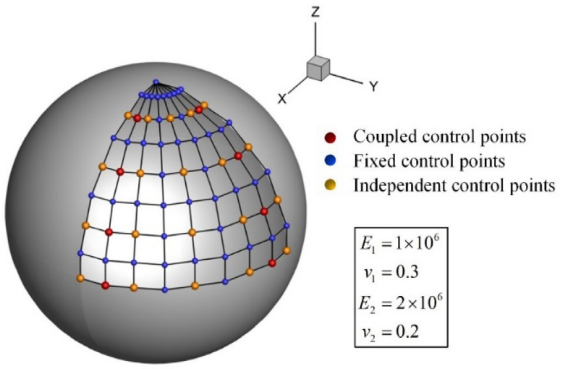

Fig. 16. Design model of spherical inclusion including 482 control points and 128 elements.

- Case I: $\sigma^0_{xx} = \sigma^0_{yy} = \sigma^0_{zz} = \sigma^0 = 10^3$;
- Case II: $\sigma^0_{xx} = 10^3, \sigma^0_{yy} = -10^3, \sigma_{zz} = 0$;

After iterative process, Table 4 gives the final values of design variables. Figs. 17 and 18 illustrate the convergence of the iteration process. The elastic energy increment will increase under identical volume. The optimized geometries and Von Mises stress distributions can be descripted as shown in Fig. 19.

5.3. Irregular circular ring inclusion

To further test the robustness of the present method, an irregular circular ring inclusion embedded in an infinite matrix is shown in Fig. 20. The design model (see Fig. 21) is converted from basic CAD model (see Fig. 20) by h-refinement with one time only on ξ parametric direction, in which a quadratic NURBS surface combines with 48 elements and 192 control points. Due to the symmetry of geometry, only five independent variables, which represent the radial distance of center point of each profile as shown in Fig. 21, are chosen as design variables. The whole control points of each profile follow the corresponding design variables. The Neumann boundary condition is $\sigma^0_{xx} = \sigma^0_{yy} = \sigma^0 = 10^3, \sigma^0_{zz} = 0$, and the constraint is that the structure volume V should not exceed 10022.52. The design mesh is refined from CAD mesh. The initial values of design variables are obtained from Fig. 21. The

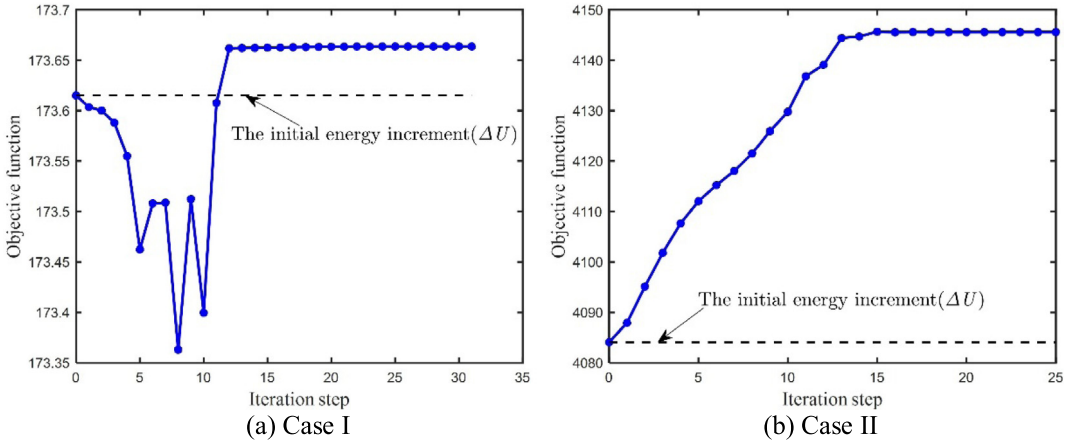

Fig. 17. The relation between objective function and iteration step.

Table 4
Design variables in spherical inclusion optimization procedure.

Index	Initial value	Lower bound	Upper bound	Final value	
				Case I	Case II
1	10.0000	8	12	9.9051	8.0000
2	10.0290	8	12	12.0000	9.8363
3	10.0290	8	12	12.0000	9.8363
4	10.0000	8	12	9.9051	8.0000
5	10.0000	8	12	9.4875	8.0000
6	10.1067	8	12	12.0000	9.9303
7	10.1067	8	12	12.0000	9.9303
8	10.0000	8	12	9.4875	8.0000
9	10.0000	8	12	8.3715	10.3199
10	10.1837	8	12	12.0000	11.1004
11	10.1837	8	12	12.0000	11.1004
12	10.0000	8	12	8.3715	10.3199
13	10.0000	8	12	8.4550	12.0000
14	10.2122	8	12	12.0000	12.0000
15	10.2122	8	12	12.0000	12.0000
16	10.0000	8	12	8.4550	12.0000

Table 5
Design variables in irregular circular ring inclusion.

Index	Initial value	Lower bound	Upper bound	Final value
1	30.0000	27	33	27.0000
2	26.1313	24	28	24.0000
3	18.2843	16	30	22.0115
4	26.1313	24	28	24.0000
5	30.0000	27	33	27.0000

lower bound and upper bound can be seen in Table 5. The objective is to maximize the elastic energy increment of the heterogeneous structure. Figs. 22 and 23 illustrate the convergence of iteration process about objective function and constrained volume. Fig. 24 presents the comparison between the unoptimized and optimized geometries about Von Mises stress distribution. The final values of design variables can be found in Table 5. The optimized shape based on NURBS geometric model can be converted into a CAD model directly in postprocessing.

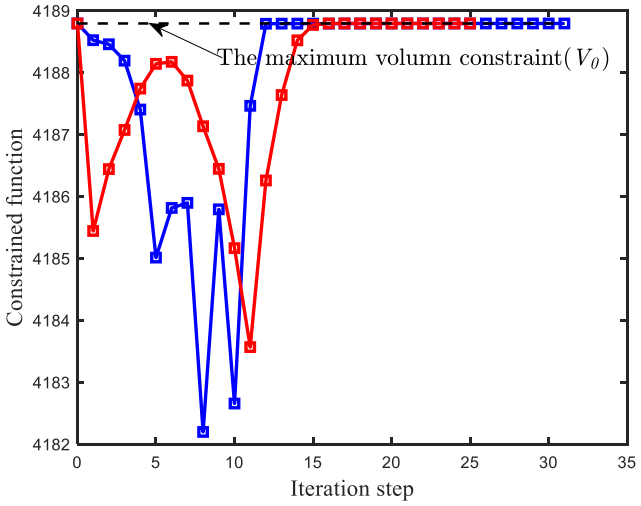

Fig. 18. The relation between constrained function and iteration step.

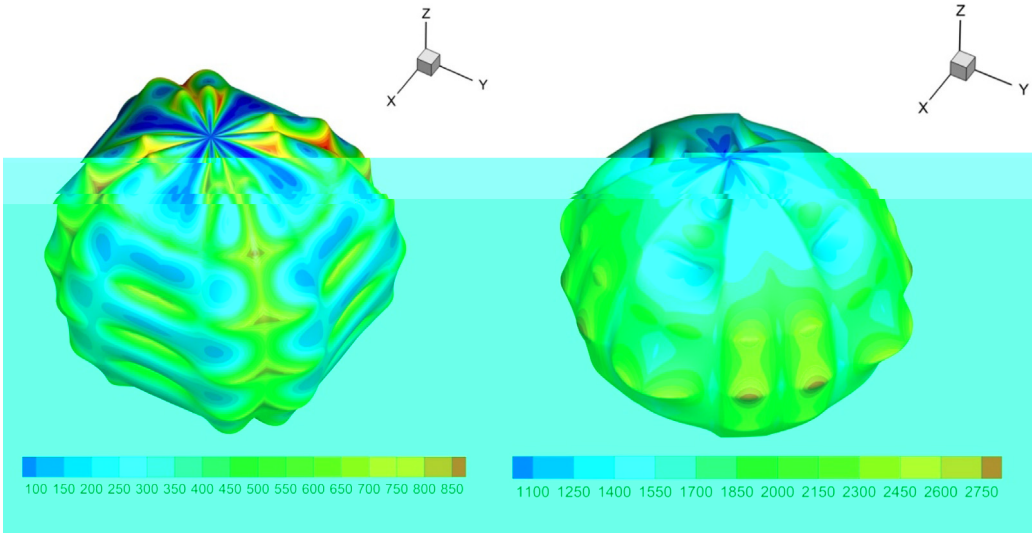

(a) Case I (b) Case II

Fig. 19. The Von Mises stress distribution for optimized geometries.

6. Conclusions

This work extended the isogeometric boundary element method (IGABEM) to the shape optimization of heterogeneous structure in elastic problems. Using the improved Greville abscissae definition in IGABEM, the corner point problem is avoided,thus the sensitivity of coefficient matrix $\mathbf{C}(\mathbf{x})$ is zero. The power series expansion method (PSEM) has been extended to evaluate the hypersingular integrals after evaluation of the singular sensitivity boundary integral and it owns more accuracy and efficiency compared with the element sub-division method (ESDM) used in the regularized boundary integral. The control points are chosen as design variables naturally, and the optimized geometry can return to CAD model without postprocessing. The elastic energy increment of composite material is chosen as objective function to optimize geometries and evaluate the error of sensitivity analysis. The robustness of the proposed algorithm has been verified by several numerical examples.

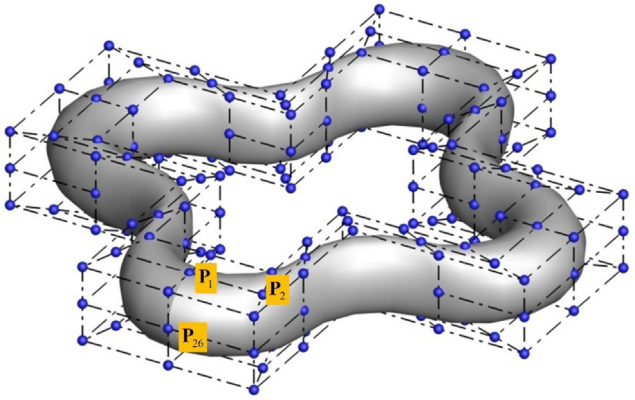

Fig. 20. CAD Model: The two knot vectors for NURBS surface are Ξ = {0, 0, 0, 1, 1, 2, 2, 3, 3, …., 9, 9, 10, 10, 11, 12, 12,} and $\Re$ = {0, 0, 0, 1, 1, 2, 2, 3, 3, 4, 4, 4}. Degree 2 is chosen in two directions. This NURBS surface can be divided into 48 patches by continuity of knot vectors. The numbers of elements and control points are 48 and 192, respectively. The coordinates of control points are (30, 0, 5) for P_1, (30, 10, 5) for P_2 and (35,0,5) for P_{26}.

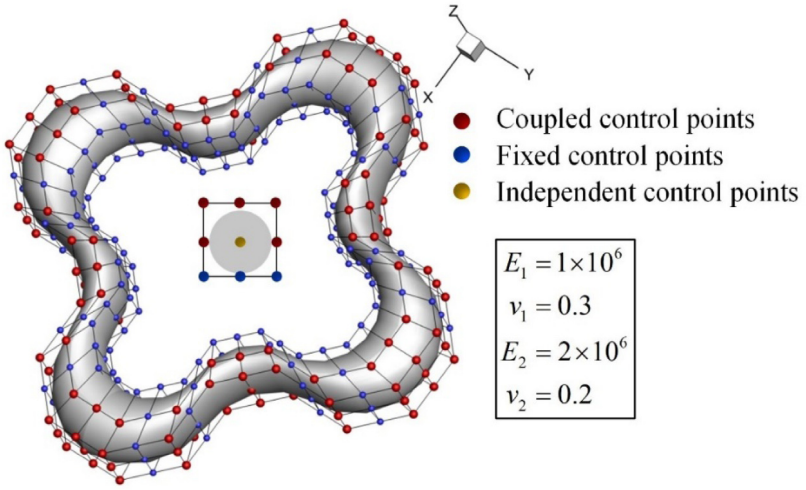

Fig. 21. Design model: The orders of NURBS surface are *p=2* and *q=2*, and the numbers of elements and control points are 96 and 441, respectively. The five radius distances are chosen as design variables.

The shape optimization for heterogeneous structure is a key step to solve large-scale engineering problems. However, due to the full populated matrices obtained by BEM, the present method requires a large amount of computation, that is, the solution time of case I in Section 5.2.2 is 3.5 days, which hinders its application in large scale problems. In the future, some accelerated algorithms such as Fast Multipole Method (FMM) [5], the wideband FMM [6], Adaptive Cross Approximation (ACA) [7], etc. must be adopted for shape optimization. The application of shape optimization of heterogeneous structure in elastic problems can be naturally extended to fluid mechanics [13], electromagnetism [14], heat conduction [15], acoustics [27,28] and so on.

This work focuses on the implementation of shape optimization for heterogeneous materials, which cannot avoid the drawbacks of IGA based NURBS. In the future, the Geometry-Independent Field approximaTion (GIFT) method [64], which allows local refinement in regions and decreases the number of control points, and other splines for boundary and fields will be adopted.

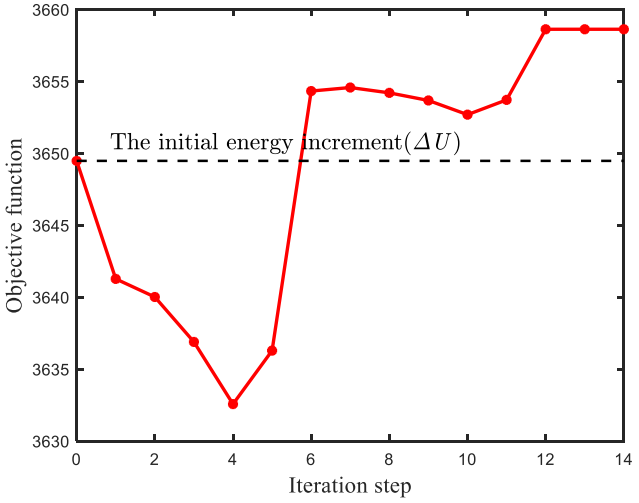

Fig. 22. The relation between objective function and iteration step.

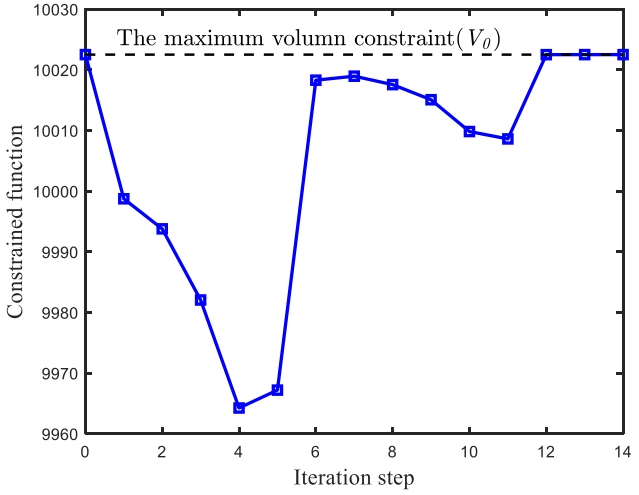

Fig. 23. The relation between constrained function and iteration step.

Declaration of competing interest

The authors declare that they have no known competing financial interests or personal relationships that could have appeared to influence the work reported in this paper.

Acknowledgment

The research is supported by the National Natural Science Foundation of China (11972085, 11672038).

Appendix A. Singularity of kernel function sensitivities

In the process of solving the sensitivity of boundary integral, we must preprocess the singularity of kernel functions and their sensitivities. In fact, sensitivity analysis of kernel functions does not change their singularity.

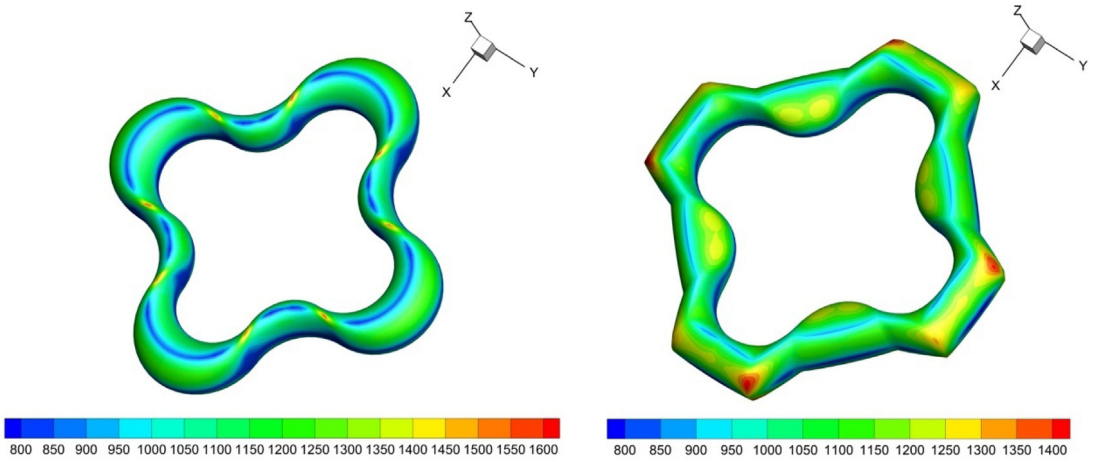

(a) Unoptimized geometry. (b) Optimized geometry.

Fig. 24. The Von Mises Stress distribution.

In order to apply PSEM in shape optimization procedure, Taylor expression is used to eliminate numerical error when the distance between source point and Gauss quadrature point is very small, i.e.

$$x_i - x_i^P = \frac{\partial x_i}{\partial \xi_K}(\xi_K - \xi_K^P) + \frac{1}{2}\frac{\partial^2 x_i}{\partial \xi_K \partial \xi_J}(\xi_K - \xi_K^P)(\xi_J - \xi_J^P) + \cdots \tag{79}$$

$$\dot{x_i} - \dot{x_i^P} = \frac{\partial \dot{x_i}}{\partial \xi_K}(\xi_K - \xi_K^P) + \frac{1}{2}\frac{\partial^2 \dot{x_i}}{\partial \xi_K \partial \xi_J}(\xi_K - \xi_K^P)(\xi_J - \xi_J^P) + \cdots \tag{80}$$

where in three-dimension problems, $K, J = 1, 2$, $\xi_K = \xi_K^P + \rho_{,K}\rho$

$$x_i - x_i^P = M_i\rho + N_i\rho^2 + O(\rho^2) \tag{81}$$

$$\dot{x_i} - \dot{x_i^P} = \dot{M}_i\rho + \dot{N}_i\rho^2 + O(\rho^2) \tag{82}$$

where

$$M_i = \frac{\partial x_i}{\partial \xi_K}\rho_{,K},\ N_i = \frac{1}{2}\frac{\partial^2 x_i}{\partial \xi_K \partial \xi_J}\rho_{,K}\rho_{,J} \tag{83}$$

$$\dot{M}_i = \frac{\partial \dot{x_i}}{\partial \xi_K}\rho_{,K},\ \dot{N}_i = \frac{1}{2}\frac{\partial^2 \dot{x_i}}{\partial \xi_K \partial \xi_J}\rho_{,K}\rho_{,J} \tag{84}$$

Meanwhile, the distance r and shape sensitivity of distance $\dot{r}$ are defined as

$$r = \sqrt{(x_i - x_i^P)(x_i - x_i^P)} = W(\rho)\rho \tag{85}$$

with

$$W(\rho) = \sqrt{M_iM_i + 2M_iN_i\rho + N_iN_i\rho^2} \tag{86}$$

and

$$\dot{r} = \frac{(\dot{x_i} - \dot{x_i^P})(x_i - x_i^P)}{r} = \mathrm{Z}(\rho)\rho \tag{87}$$

with

$$\mathrm{Z}(\rho) = \frac{(\dot{M}_i + \dot{N}_i\rho)(M_i + N_i\rho)}{W(\rho)} \tag{88}$$

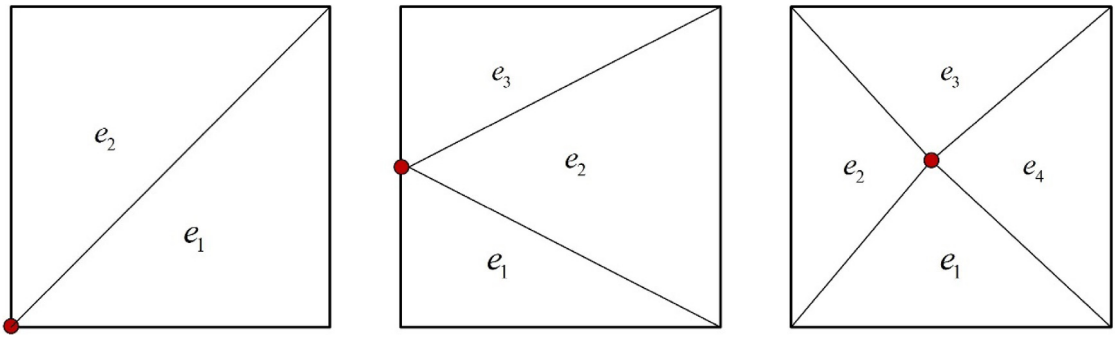

Fig. 25. The triangular element sub-division method.

Then, the other parameters are shown as follows:

$$\dot{r_{,i}} = \frac{(\dot{x_i} - \dot{x_i^P})r - (x_i - x_i^P)\dot{r}}{r^2} = \frac{(\dot{M}_i + \dot{N}_i\rho)W(\rho) - (M_i + N_i\rho)Z(\rho)}{W^2(\rho)} \tag{89}$$

$$\frac{\dot{r}}{r} = \frac{Z(\rho)}{W(\rho)} \tag{90}$$

When source point approaches or coincides with field point, $\rho \mapsto 0$, then

$$\dot{r} = 0 \tag{91}$$

$$r_{,i} = \frac{M_i}{\sqrt{M_j M_j}} \tag{92}$$

$$\dot{r_{,i}} = \frac{\dot{M}_i(M_j M_j)^{1/2} - M_i(M_s\dot{M}_s)}{(M_k M_k)} \tag{93}$$

$$\frac{\dot{r}}{r} = \frac{M_i\dot{M}_i}{M_j M_j} \tag{94}$$

The core of power series expansion is to consider $r_{,i}$, $\dot{r_{,i}}$ and $\dot{r}/r$ as a whole, and the sensitivity of kernel functions' singular order λ is the same as that of $\mathbf{U}(\mathbf{x}, \mathbf{y})$ and $\mathbf{T}(\mathbf{x}, \mathbf{y})$.

Appendix B. The element sub-division method based on the regularized boundary integral equation

In the process of shape optimization for homogeneous materials, the regularized boundary integral equation is the common method to avoid corner point problem, especially for the sensitivity of the coefficient matrix $\mathbf{C}(\mathbf{x})$. Thus, the boundary integral equations (19) and (48) can be reformulated as

$$\int_S \mathbf{T}(\mathbf{x}, \mathbf{y})[\mathbf{u}(\mathbf{x}) - \mathbf{u}(\mathbf{y})]dS + B\mathbf{u}(\mathbf{x}) = B\mathbf{u}^0(\mathbf{x}) - \int_S \mathbf{U}(\mathbf{x}, \mathbf{y})\mathbf{t}(\mathbf{y})dS \tag{95}$$

and

$$\int_S \left\{\dot{\mathbf{T}}(\mathbf{x}, \mathbf{y})[\mathbf{u}(\mathbf{x}) - \mathbf{u}(\mathbf{y})] + \mathbf{T}(\mathbf{x}, \mathbf{y})[\dot{\mathbf{u}}(\mathbf{x}) - \dot{\mathbf{u}}(\mathbf{y})]\right\} dS + \int_S \mathbf{T}(\mathbf{x}, \mathbf{y})[\mathbf{u}(\mathbf{x}) - \mathbf{u}(\mathbf{y})]d\dot{S}$$
$$+ B\dot{\mathbf{u}}(\mathbf{x}) = B\dot{\mathbf{u}}^{\mathbf{0}} - \int_S [\dot{\mathbf{U}}(\mathbf{x}, \mathbf{y})\mathbf{t}(\mathbf{y})dS + \mathbf{U}(\mathbf{x}, \mathbf{y})\dot{\mathbf{t}}(\mathbf{y})dS + \mathbf{U}(\mathbf{x}, \mathbf{y})\mathbf{t}(\mathbf{y})d\dot{S}] \tag{96}$$

The singularity order of kernel function and its sensitivity can be decreased once, i.e.

$$\mathbf{T}(\mathbf{x}, \mathbf{y})[\mathbf{u}(\mathbf{x}) - \mathbf{u}(\mathbf{y})] \sim o(\frac{1}{r^2})o(r) = o(\frac{1}{r}) \tag{97}$$

and

$$\left.\begin{matrix}\dot{\mathbf{T}}(\mathbf{x},\mathbf{y})[\mathbf{u}(\mathbf{x})-\mathbf{u}(\mathbf{y})]\\ \mathbf{T}(\mathbf{x},\mathbf{y})[\dot{\mathbf{u}}(\mathbf{x})-\dot{\mathbf{u}}(\mathbf{y})]\end{matrix}\right\} \sim o(\frac{1}{r^2})o(r)=o(\frac{1}{r}) \tag{98}$$

Consequently, the regularized boundary integral equation only contains weakly integrals, which can be evaluated by the triangular element sub-division method [53,65] as shown in Fig. 25.

References

[1] O.C. Zienkiewicz, R.L. Taylor, J.Z. Zhu, The Standard Discrete System and Origins of the Finite Element Method, Butterworth-Heinemann, Oxford, 2013.

[2] T.A. Cruse, A direct formulation and numerical solution of the general transient elastodynamic problem. II, J. Math. Anal. Appl. 22 (1968) 341–355.

[3] T.A. Cruse, Numerical solutions in three dimensional elastostatics, Int. J. Solids Struct. 5 (1969) 1259–1274.

[4] J.A. Cottrell, T.J.R. Hughes, Y. Bazilevs, Isogeometric Analysis: Toward Integration of CAD and FEA, Wiley, UK, 2009.

[5] L. Greengard, V. Rokhlin, A fast algorithm for particle simulations, J. Comput. Phys. 73 (1987) 325–348.

[6] C.J. Zheng, C.X. Bi, C.Z. Zhang, Y.B. Zhang, H.B. Chen, Fictitious eigenfrequencies in the BEM for interior acoustic problems, Eng. Anal. Bound. Elem. 104 (2019) 170–182.

[7] M. Bebendorf, Approximation of boundary element matrices, Numer. Math. 86 (2000) 565–589.

[8] G. Beylkin, R. Coifman, V. Rokhlin, Fast wavelet transforms and numerical algorithms I, Commun. Pure Appl. Math. Comput. 44 (2010) 141–183.

[9] J.R. Phillips, J.K. White, A precorrected-FFT method for electrostatic analysis of complicated 3-d structures, IEEE Trans. Comput.-Aided Des. Integr. Circuits Syst. 16 (1997) 1059–1072.

[10] T.J.R. Hughes, J.A. Cottrell, Y. Bazilevs, Isogeometric analysis: CAD, finite elements, nurbs, exact geometry and mesh refinement, Comput. Methods Appl. Mech. Engrg. 194 (2005) 4135–4195.

[11] W.A. Wall, M.A. Frenzel, C. Cyron, Isogeometric structural shape optimization, Comput. Methods Appl. Mech. Engrg. 197 (2008) 2976–2988.

[12] X.P. Qian, Full analytical sensitivities in NURBS based isogeometric shape optimization, Comput. Methods Appl. Mech. Engrg. 199 (2010) 2059–2071.

[13] P. Nortoft, J. Gravesen, Isogeometric shape optimization in fluid mechanics, Struct. Multidiscip. Optim. 48 (2013) 909–925.

[14] S.W. Lee, J. Lee, S. Cho, Isogeometric shape optimization of ferromagnetic materials in magnetic actuators, IEEE Trans. Magn. 52 (2016).

[15] Z.P. Wang, S. Turteltaub, M. Abdalla, Shape optimization and optimal control for transient heat conduction problems using an isogeometric approach, Comput. Struct. 185 (2017) 59–74.

[16] Q. Hu, F. Chouly, P. Hu, G. Cheng, S.P.A. Bordas, Skew-symmetric nitsche's formulation in isogeometric analysis: Dirichlet and symmetry conditions, patch coupling and frictionless contact, Comput. Methods Appl. Mech. Engrg. 341 (2018) 188–220.

[17] V.P. Nguyen, P. Kerfriden, M. Brino, S.P.A. Bordas, E. Bonisoli, Nitsche's method for two and three dimensional NURBS patch coupling, Comput. Mech. 53 (2014) 1163–1182.

[18] M.J. Peake, J. Trevelyan, G. Coates, Extended isogeometric boundary element method (XIBEM) for three-dimensional medium-wave acoustic scattering problems, Comput. Methods Appl. Mech. Engrg. 284 (2015) 762–780.

[19] K.V. Kostas, A.I. Ginnis, C.G. Politis, P.D. Kaklis, Ship-hull shape optimization with a T-spline based BEM-isogeometric solver, Comput. Methods Appl. Mech. Engrg. 284 (2015) 611–622.

[20] L. Coox, F. Greco, O. Atak, D. Vandepitte, W. Desmet, A robust patch coupling method for NURBS-based isogeometric analysis of non-conforming multipatch surfaces, Comput. Methods Appl. Mech. Engrg. 316 (2017) 235–260.

[21] A.I. Ginnis, K.V. Kostas, C.G. Politis, P.D. Kaklis, K.A. Belibassakis, T.P. Gerostathis, M.A. Scott, T.J.R. Hughes, Isogeometric boundary-element analysis for the wave-resistance problem using T-splines, Comput. Methods Appl. Mech. Engrg. 279 (2014) 425–439.

[22] Y.J. Wang, D.J. Benson, A.P. Nagy, A multi-patch nonsingular isogeometric boundary element method using trimmed elements, Comput. Mech. 56 (2015) 173–191.

[23] V.P. Nguyen, C. Anitescu, S.P.A. Bordas, T. Rabczuk, Isogeometric analysis: An overview and computer implementation aspects, Math. Comput. Simulation 117 (2015) 89–116.

[24] A. Yadav, R.K. Godara, G. Bhardwaj, A review on XIGA method for computational fracture mechanics applications, Eng. Fract. Mech. 230 (2020) 107001.

[25] K. Li, X.P. Qian, Isogeometric analysis and shape optimization via boundary integral, Comput. Aided Des. 43 (2011) 1427–1437.

[26] H. Lian, P. Kerfriden, S.P.A. Bordas, Implementation of regularized isogeometric boundary element methods for gradient-based shape optimization in two-dimensional linear elasticity, Internat. J. Numer. Methods Engrg. 106 (2016) 972–1017.

[27] C. Liu, L.L. Chen, W.C. Zhao, H.B. Chen, Shape optimization of sound barrier using an isogeometric fast multipole boundary element method in two dimensions, Eng. Anal. Bound. Elem. 85 (2017) 142–157.

[28] L.L. Chen, H. Lian, Z. Liu, H.B. Chen, E. Atroshchenko, S.P.A. Bordas, Structural shape optimization of three dimensional acoustic problems with isogeometric boundary element methods, Comput. Methods Appl. Mech. Engrg. 355 (2019) 926–951.

[29] H. Lian, P. Kerfriden, S.P.A. Bordas, Shape optimization directly from CAD: An isogeometric boundary element approach using T-splines, Comput. Methods Appl. Mech. Engrg. 317 (2017) 1–41.

[30] X. Peng, E. Atroshchenko, P. Kerfriden, S.P.A. Bordas, Isogeometric boundary element methods for three dimensional static fracture and fatigue crack growth, Comput. Methods Appl. Mech. Engrg. 316 (2017) 151–185.
[31] X. Peng, E. Atroshchenko, P. Kerfriden, S.P.A. Bordas, Linear elastic fracture simulation directly from CAD: 2D NURBS-based implementation and role of tip enrichment, Int. J. Fract. 204 (2016) 1–24.
[32] T.Z. Chen, B. Wang, Z.Z. Cen, Z.S. Wu, A symmetric Galerkin multi-zone boundary element method for cohesive crack growth, Eng. Fract. Mech. 63 (1999) 591–609.
[33] X.W. Gao, K. Yang, Interface integral BEM for solving multi-medium elasticity problems, Comput. Methods Appl. Mech. Engrg. 198 (2009) 1429–1436.
[34] J.C.F. Telles, A self-adaptive co-ordinate transformation for efficient numerical evaluation of general boundary element integrals, Internat. J. Numer. Methods Engrg. 24 (1987) 959–973.
[35] H.B. Chen, P. Lu, M.G. Huang, F.W. Williams, An effective method for finding values on and near boundaries in the elastic BEM, Comput. Struct. 69 (1998) 421–431.
[36] Y. Liu, T.J. Rudolphi, Some identities for fundamental solutions and their applications to weakly-singular boundary element formulations, Eng. Anal. Bound. Elem. 8 (1991) 301–311.
[37] Y.J. Liu, T.J. Rudolphi, New identities for fundamental solutions and their applications to non-singular boundary element formulations, Comput. Mech. 24 (1999) 286–292.
[38] Y.J. Liu, On the simple-solution method and non-singular nature of the BIE/BEM — a review and some new results, Eng. Anal. Bound. Elem. 24 (2000) 789–795.
[39] L. Ma, A.M. Korsunsky, A note on the Gauss-Jacobi quadrature formulae for singular integral equations of the second kind, Int. J. Fract. 126 (2004) 399–405.
[40] O. Huber, A. Lang, G. Kuhn, Evaluation of the stress tensor in 3D elastostatics by direct solving of hypersingular integrals, Internat. J. Numer. Methods Engrg. 39 (1993) 2555–2573.
[41] G. Karami, D. Derakhshan, An efficient method to evaluate hypersingular and supersingular integrals in boundary integral equations analysis, Eng. Anal. Bound. Elem. 23 (1999) 317–326.
[42] M. Cerrolaza, E. Alarcon, A bi-cubic transformation for the numerical evaluation of the Cauchy principal value integrals in boundary methods, Internat. J. Numer. Methods Engrg. 28 (1989) 987–999.
[43] Z. Niu, X. Wang, H. Zhou, Non-singular algorithm for the evaluation of the nearly singular integrals in boundary element methods, Chinese J. Appl. Mech. 18 (2001) 1–8.
[44] H.R. Kutt, The numerical evaluation of principal value integrals by finite-part integration, Numer. Math. 24 (1975) 205–210.
[45] X.W. Gao, An effective method for numerical evaluation of general 2D and 3D high order singular boundary integrals, Comput. Methods Appl. Mech. Engrg. 199 (2010) 2856–2864.
[46] Y.P. Gong, C.Y. Dong, X.C. Qin, An isogeometric boundary element method for three dimensional potential problems, J. Comput. Appl. Math. 313 (2017) 454–468.
[47] K. Otsuka, C.M. Wayman, Shape Memory Materials, Cambridge University Press, USA, 1998.
[48] J.W. Eshelby, Elastic inclusions and inhomogeneities, Progr. Solid Mech. 2 (1961) 87–140.
[49] G. Farin, J. Hoschek, M.-S. Kim, Handbook of Computer Aided Geometric Design, Elsevier, Amsterdam, 2002.
[50] R.N. Simpson, S.P.A. Bordas, J. Trevelyan, T. Rabczuk, A two-dimensional isogeometric boundary element method for elastostatic analysis, Comput. Methods Appl. Mech. Engrg. 209–212 (2012) 87–100.
[51] C. Brebbia, J. Dominguez, Boundary Elements: An Introductory Course, Computational Mechanics Publ., London, 1989.
[52] C.Y. Dong, S.H. Lo, Y.K. Cheung, Interaction between coated inclusions and cracks in an infinite isotropic elastic medium, Eng. Anal. Bound. Elem. 27 (2003) 871–884.
[53] Y.J. Wang, D.J. Benson, Multi-patch nonsingular isogeometric boundary element analysis in 3D, Comput. Methods Appl. Mech. Engrg. 293 (2015) 71–91.
[54] L.F. Kallivokas, T. Juneja, J. Bielak, A symmetric Galerkin BEM variational framework for multi-domain interface problems, Comput. Methods Appl. Mech. Engrg. 194 (2005) 3607–3636.
[55] B. Marussig, J. Zechner, G. Beer, T.-P. Fries, Fast isogeometric boundary element method based on independent field approximation, Comput. Methods Appl. Mech. Engrg. 284 (2015) 458–488.
[56] R.N. Simpson, S.P.A. Bordas, H. Lian, J. Trevelyan, An isogeometric boundary element method for elastostatic analysis: 2D implementation aspects, Comput. Struct. 118 (2013) 2–12.
[57] E. Kita, H. Tanie, Shape optimization of continuum structures by genetic algorithm and boundary element method, Eng. Anal. Bound. Elem. 19 (1997) 129–136.
[58] K.V. Kostas, A.I. Ginnis, C.G. Politis, P.D. Kaklis, Shape-optimization of 2D hydrofoils using an isogeometric BEM solver, Comput. Aided Des. 82 (2017) 79–87.
[59] M.M. Mafarja, S. Mirjalili, Hybrid whale optimization algorithm with simulated annealing for feature selection, Neurocomputing 260 (2017) 302–312.
[60] T. Okuno, M. Fukushima, An interior point sequential quadratic programming-type method for log-determinant semi-infinite programs, J. Comput. Appl. Math. 376 (2020) 112784.
[61] C.Y. Dong, A more general interface integral formula for the variation of matrix elastic energy of heterogeneous materials, in: Mechanics and Engineering - Numerical Computation and Data Analysis, Beijing, 2019, pp. 95–98.
[62] T. Hirschler, R. Bouclier, A. Duval, T. Elguedj, J. Morlier, Isogeometric sizing and shape optimization of thin structures with a solid-shell approach, Struct. Multidiscip. Optim. 59 (2019) 767–785.
[63] J. Kiendl, R. Schmidt, R. Wüchner, K.U. Bletzinger, Isogeometric shape optimization of shells using semi-analytical sensitivity analysis and sensitivity weighting, Comput. Methods Appl. Mech. Engrg. 274 (2014) 148–167.

[64] E. Atroshchenko, S. Tomar, G. Xu, S.P.A. Bordas, Weakening the tight coupling between geometry and simulation in isogeometric analysis: From sub- and super-geometric analysis to geometry-independent field approximation (GIFT), 114, 2018, pp. 1131–1159.
[65] J.C. Lachat, J.O. Watson, Effective numerical treatment of boundary integral equations: a formulation for three-dimensional elastostatics, Internat. J. Numer. Methods Engrg. 10 (1976) 991–1005.